CLOUD MORPHOLOGY AND DYNAMICS IN SATURN'S NORTHERN POLAR REGION

Arrate Antuñano[1], Teresa del Río-Gaztelurrutia[1], Agustín Sánchez-Lavega[1] and Javier Rodríguez-Aseguinolaza[1,2]

[1]Departamento de Física Aplicada I, Escuela de Ingeniería de Bilbao, Universidad del País Vasco, Bilbao, Spain.
[2] CIC Energigune, Albert Einstein 48, 01510 – Miñano (Álava), Spain.

Abstract

We present a study of the cloud morphology and motions in the north polar region of Saturn, from latitude ~ 70ºN to the pole based on Cassini ISS images obtained between January 2009 and November 2014. This region shows a variety of dynamical structures: the permanent hexagon wave and its intense eastward jet, a large field of permanent "puffy" clouds with scales from 10 – 500 km, probably of convective origin, local cyclone and anticyclones vortices with sizes of ~1,000 km embedded in this field, and finally the intense cyclonic polar vortex. We report changes in the albedo of the clouds that delineate rings of circulation around the polar vortex and the presence of "plume-like" activity in the hexagon jet, in both cases not accompanied with significant variations in the corresponding jets. No meridional migration is observed in the clouds forming and merging in the field of puffy clouds, suggesting that their mergers do not contribute to the maintenance of the polar vortex. Finally, we analyze the dominant growing modes for barotropic and baroclinic instabilities in the hexagon jet, showing that a mode 6 barotropic instability is dominant at the latitude of the hexagon.

Highlights

- We study the North Polar Region of Saturn from 70º to the pole based on Cassini ISS images from January 2009 to November 2014.

- We find local anticyclonic and cyclonic vortices of 1000 km to 3500 km size and a large "puffy" cloud field of sizes 10 to 300 km.

- We report a presence of "plume-like" activity inside the Hexagon jet.

- The North Polar Vortex suffered drastic changes in the cloud morphology between November 2012 and September 2014, but not in the zonal wind profile.

- We present a study of barotropic and baroclinic instability for the Hexagon and its counterpart in the south at 70.4ºS. Wavenumber six arises naturally as a barotropic instability, but not as a baroclinic one.

1. Introduction

Saturn's polar regions present a wide variety of cloud morphologies at visual wavelengths, some of them unique in the solar system. In the north, a remarkable hexagonal feature can be observed at 75° planetocentric latitude. This feature, which encloses a fast and narrow eastward jet with peak speed ~100 ms^{-1} , was first observed in 1980 and 1981 in Voyager I and II flybys (Godfrey, 1988) and has proven to be a stable feature. It was re-observed by ground-based telescopes and Hubble Space Telescope between 1990 and 1995 (Sánchez-Lavega et al., 1993; Caldwell et al., 1993) and later by Cassini, first, in Saturn's late northern winter, with the composite infrared spectrometer (CIRS) in 2007-2008 (Fletcher et al., 2008), then by the visual and infrared mapping spectrometer (VIMS) (Baines et al., 2009) and finally by the imaging science system (ISS) (Sánchez-Lavega et al., 2014; Antuñano et al., 2015; Sayanagi et al., 2016).

At the time of Voyager flybys, an elliptical anticyclone of 7000-10000 km long, named North Polar Spot (NPS), was observed just outside the hexagonal feature. This large anticyclone, reddish in color (Hunt and Moore, 1982), was re-observed with ground-based telescopes in 1995 (Sánchez-Lavega et al., 1997). The presence of the NPS impinging on the eastward jet enclosed by the hexagon was proposed as the way of the creation of the hexagonal feature (Allison et al., 1990). However, this feature was not observed in Cassini images (Fletcher et al., 2008; Baines et al., 2009; Sánchez-Lavega et al., 2014; Antuñano et al., 2015) whereas the hexagon persisted. The absence of the NPS in Cassini images showed that its presence is not necessary for the hexagon to remain. Furthermore, it has been observed that this hexagonal feature has an extremely steady rotation period, its vertices moving with a velocity relative to Saturn System III (Desch and Kaiser, 1981; Seidelmann et al., 2007) of just -0.036 ± 0.004 ms^{-1} (Sánchez-Lavega et al., 2014), which led to interpretation of the hexagon as a vertically trapped Rossby wave (Allison et al., 1990; Sánchez-Lavega et al., 2014).

The arrival of Cassini at Saturn in 2004 allowed the study of these regions in more detail. A circular and highly stable cyclonic polar vortex, first observed as an increase on the temperature maps by Fletcher et al. (2008), was revealed in visible images after Saturn's equinox, when Saturn's north pole started to be illuminated by sunlight. This vortex is surrounded by a fast eastward jet with a velocity peak of 140-160 ms^{-1} at 88.5°N planetocentric latitude (Sayanagi et al., 2013; Antuñano et al., 2015; Sayanagi et al., 2016; Sayanagi et al., 2017). The north polar vortex is counterpart to the polar vortex of similar shape and size that was observed earlier in Saturn's south polar region, first in thermal-infrared images obtained from Earth (Orton and Yanamandra-Fisher, 2005) and later by Cassini images (Sánchez-Lavega et al., 2006; Dyudina et al., 2008; Antuñano et al., 2015; Sayanagi et al., 2017), also surrounded by a narrow and fast prograde jet with a velocity peak of ~160 ms^{-1} located at 88.5°S. This analogy between north and south does not extend to lower latitudes, since no hexagonal feature is observed on the quasi-symmetric jet located in the south (Sánchez-Lavega et al., 2002; Antuñano et al., 2015).

In this work we extend the analysis of Saturn northern region to include new Cassini ISS images of the north polar region obtained in the period from June 2013 to November 2014 and we include a theoretical analysis of the barotropic and baroclinic instabilities of the hexagonal jet. The structure of the paper is as follows. In section 2 we summarized our data and methodology. In section 3, we present albedo changes in the clouds forming the north polar vortex and the dynamical behavior of the vortex in relation to these changes.

In sections 4 we analyze the region between the hexagon and the polar jet, and we report the presence of closed vortices and a broad field of "puffy" clouds. In section 5 we report on transient dynamical features observed in the hexagon jet. In section 6, we analyze the growing rates for barotropic and baroclininc instabilities at the hexagonal jet and its counterpart in the south at 70.4ºS and in section 7 we summarize our conclusions.

2. Images used and Methodology

Different sets of high-resolution images obtained by the Imaging Science System (ISS) (Porco et al., 2004) onboard Cassini spacecraft were used in this study: (a) two sets of Wide Angle Camera (WAC) images using Continuum Band 2 filter (CB2) in July 2013 and November 2013, for the study of the cloud morphology in the Hexagon; (b) A set of WAC CB2 images taken in April 2009 and a single image taken with the same configuration in June 2013, for the analysis of the morphology and statistics of the compact cloud field in the north polar region and (c) two sets of Narrow Angle Camera (NAC) images taken using CB2 and Methane 2 (MT2) filters in April 2014 and September 2014 for the study of the dynamics of the polar vortex. Moreover, in the study of the variation of the cloud morphology of the polar vortex, in addition to the CB2 and MT2 filters, we also used images captured using ultraviolet (UV3), red (RED), blue (BL1) and green (GRN) filters. We concentrate on CB2 images for the study of the cloud morphology in the Hexagon and the analysis of the compact cloud fields because they show features in these regions with the highest contrast.

Each selected image was navigated using the Planetary Laboratory for Image Analysis software (PLIA) (Hueso et al., 2010). This software allows the user to correct the navigation manually by adjusting the position of the pole or fitting the limb. Once the images were navigated, they were polar projected using the software PLIA, which implements an azimuthally equidistant polar projection (Snyder, 1987).

With the aim of obtaining an accurate wind profile of the north polar vortex and the north polar region, we used two different techniques of wind measurements: (a) visual cloud tracking and (b) a two-dimensional brightness correlation algorithm (Hueso et al., 2009). This semi-automatic correlation algorithm allows the researcher to validate, correct or ignore the identifications manually. This is particularly important at latitudes close to the poles, where features move fast and undergo rapid changes in morphology.

Visual cloud tracking was mainly used to obtain wind vectors at the north polar vortex on selected targets, from 87°N latitude to the pole, and to measure local motions of smaller singular vortices found in the polar region. In the case of the north polar vortex, CB2 images were polar projected from 85°N to 90°N latitude with a map-projection meridional resolution of 0.005 °/pixel. Image pairs measured using this method were separated by time intervals of 39-45 minutes.

The two-dimensional brightness correlation algorithm technique was used for two different purposes. First, we confirmed the visual cloud tracking measurements of the north polar vortex and extended the wind measurements of the CB2 pairs separated by 39-45 minutes to lower latitudes. For the analysis of the north polar vortex, we used polar projection maps from 77°N to the pole with a map-projection meridional resolution of 0.01 °/pixel and boxes of 50x50 pixels in the correlation algorithm with a search area of 80x80 pixels. This choice allows us to extend the zonal and meridional wind profiles of the polar vortex down to, at least, the peak of the westward jet at 80°N, where 0.01 °/pixel of meridional resolution is enough to obtain a wind profile with an estimated mean standard deviation of ± 7ms^{-1}. The highest density of wind vectors obtained by this method corresponds to latitudes between 77°N and 87°N; however, a small number of wind vectors were also obtained above 87°N. Second, we studied the dynamics inside the hexagon jet and its relationship with the cloud morphology in that region. In this case, we used polar projection maps from 70°N to 90°N with a map-projection meridional resolution of 0.02 °/pixel with boxes of 60x60 pixels and a search area of 80x80 pixels. Finally, to discuss the evolution of the cloud morphology of the north polar vortex, we built polar-projection maps of images captured with additional filters, covering latitudes from 87°N to 90°N with a map-projection meridional resolution of 0.005 °/pixel. All the latitudes defined in this paper are planetocentric latitudes.

Errors in the sizes of different features are estimated taking into account the resolution of the image and the uncertainty in pointing to their limits. Errors in wind profiles are calculated as the standard deviation of all measurements within a latitudinal bin. Finally, errors in vorticity and divergence maps are estimated calculating the differences in the maps after introducing a random noise related to the uncertainty of individual measurements.

3. The North Polar Vortex

A long-lived and dynamically stable vortex is present in both poles of Saturn, with peak velocities of 140-160 ms^{-1} at 88.5° (north and south) (Sánchez-Lavega et al., 2006; Fletcher et al., 2008; Dyudina et al., 2008; Baines et al., 2009; Sayanagi et al., 2013; Antuñano et al., 2015; Sayanagi et al., 2016; Sayanagi et al., 2017). In Saturn's northern summer, Cassini ISS instrument obtained various sets of high-resolution images which allowed to determine the zonal winds in the region (Sayanagi et al., 2013; Antuñano et al., 2015; Sayanagi et al., 2016; Sayanagi et al., 2017) and proved the morphology of the vortex to be highly variable, evolving in a remarkable way.

In Figure 1, we present polar projections from 87°N to 90°N latitude, showing the north polar vortex in four different epochs and for six different wavelengths. If we take into consideration the images of November 2012 and June 2013, it becomes apparent that the vortex is a depressed region of the atmosphere. The continuum band filter CB2, penetrating through the upper haze, senses the top of the ammonia clouds and shows cloud features with very high contrast (West et al., 2009). Not only clouds at the center of the vortex appear to be deeper in the feature, but we can also see the shadow of the vortex "wall". On the other hand, methane band (MT2) images do not go through the upper haze that is always present at Saturn's polar regions, and they show a dark region without any contrasted features due to increased methane absorption. Only the highest clouds can be seen in this filter. Similarly, Rayleigh scattering by the haze makes the central region bright relative to surroundings when seen through ultraviolet (UV3) filters. Other filters (BL1, GRN, and RED) provide a transition from the penetrating to the highly absorbing filters. A study in progress will unfold the precise vertical structure of the region, analyzing the reflectivity of different regions of the vortex in different wavelengths.

The brightness temperature maps at 150 mbar from Fletcher et al. (2015) showed a seasonal warming of the north pole from November 2012 to September 2014. As can be observed in Figure 1, the cloud morphology of the vortex varied substantially over the same period. In Cassini ISS images, while in November 2012 and June 2013 the polar cyclone presented an eye-like structure, with spiraling bright clouds surrounding the eye (Antuñano et al., 2015; Sayanagi et al., 2016; Sayanagi et al., 2017), images from November 2012 showed a brighter area at the center of the polar vortex, not present in June 2013. Images from April 2014 showed a dark, almost circular cloud free area of approximately 0.3º radius at the center of the vortex, encircled by a brighter spiral-like region down to 89°N, and surrounded by a cloud-free dark ring down to 88.7° latitude. This remarkable dark ring, not observed in previous images, is encircled by a brighter spiral area covering latitudes down to 87.7°N. MT2 images of April 2014 showed a circular dark region centered at the pole and extending down to 88.6°, the outer region of the dark ring in CB2, with a few brighter features between 89.6° and 89.2°N, corresponding to the inner spiral-like region and suggestive of the presence of higher clouds in the region when compared with the images of June 2013. In UV images, this dark circular region is bright and extends down to the same latitude, 88.6°N. By September 2014, CB2 images do not have a dark cloud-free area at the center of the vortex and instead, a bright circular area centered at the pole extends down to 89.2°N. There is still a cloud-free dark ring surrounding this bright area, but it has become wider, extending 0.5° in latitude down to 88.7°N. To the south, the bright region observed in April looks darker and flatter in September. Note that the southern boundary of the bright area at the center of the vortex in September 2014 is to the north of the equivalent bright area in April, making the bright area in the center of the vortex smaller and the cloud-free dark ring wider, but extending to the same latitude. MT2 images show a circular dark region centered at the pole and extending to 88.7°N, with a narrow (0.3° wide) brighter region at 89.5°N where some cloud morphology is apparent. UV images of this epoch show again a circular bright region centered at the pole and extending down to 88.7°N. In summary, the north polar vortex showed in just two years the development and dissipation of clouds in rings at different latitudes or distances from its center while preserving its general behavior as a low region with few clouds (a hole like structure) as revealed by methane-band and ultraviolet images.

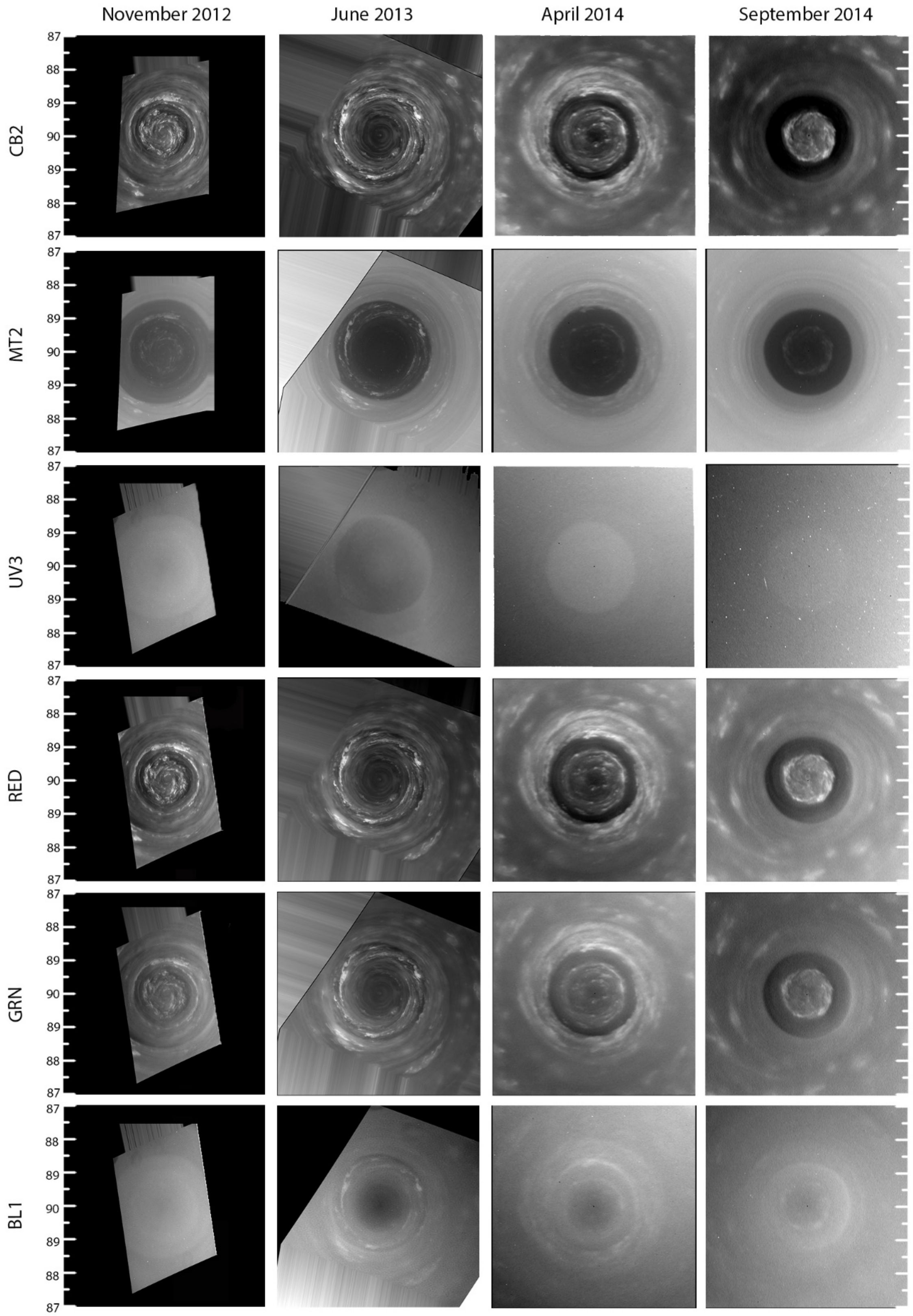

Figure 1. Polar projections from 87°N to the pole for four different epochs (November 2012, June 2013, April 2014 and September 2014) and six different filters. The radius of the latitude circle is indicated on left of each image sequence (in degrees).

With the aim of exploring if the variability of the cloud morphology is correlated to a variability of the zonal velocities, we have measured horizontal winds in April and

September 2014 and we have compared them with the zonal winds measured in June 2013 (Antuñano et al., 2015). We used two new image pairs: (a) one CB2 image pair from April 2014, separated by 38.77 minutes and (b) one CB2 image pair from September 2014 separated by 45.33 minutes. In total, we obtained ~3323 wind vectors from 85°N to the pole. Data for each epoch and filter was averaged in 0.2° latitude bins. The results are shown in Figure 2, and they reveal that despite the changes in the cloud morphology of the polar vortex between November 2012 and September 2014, the zonal and meridional wind velocity profiles do not change, reaching zonal velocities of 145 ± 18 ms^{-1} at ~88.5ºN in CB2 images, in accordance with Antuñano et al. (2015).

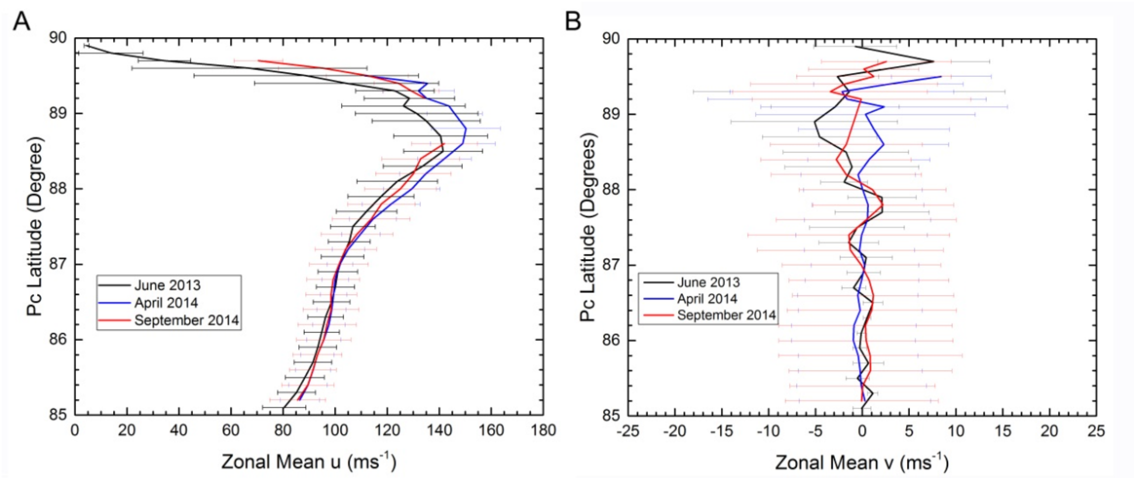

Figure 2. Zonal (a) and meridional (b) wind profiles of the north polar vortex from 85°N to the pole at three different epochs: June 14 2013 (black) (Antuñano et al., 2015), April 2 2014 (blue) and September 10 2014 (red).

Relative vorticity and divergence maps of the NPV for June 2013, April 2014 and September 2014 are presented in Figure 3. These maps show that the relative vorticity does not change significantly, and that, within error, the divergence is zero. All maps have been computed interpolating the wind data into a regular grid of ~190 km (~0.2º) and averaged over ~760 km, instead of the lower resolution interpolation and stronger smoothing performed in Antuñano et al. (2015). This is due to the fact that we focus on the north polar vortex only.

The peak velocity and relative vorticity reported here are smaller by about 10% and 40%, respectively, than the values reported by Sayanagi et al. (2017). However, the difference in the zonal velocity might be due to the higher resolution images (2 km/pixel instead of 4-16 km/pixel) and weaker spatial averaging used by Sayanagi et al. (2017), while the large difference in the relative vorticity comes from the smoothing applied here.

In summary, we have not detected any significant variation in the horizontal wind structure that can explain the differences in morphology of the region. It is likely that the cloud changes are caused by temperature changes or by vertical motions, but if this is the case, the signature of these motions on the divergence is too low to be detected at the available resolution.

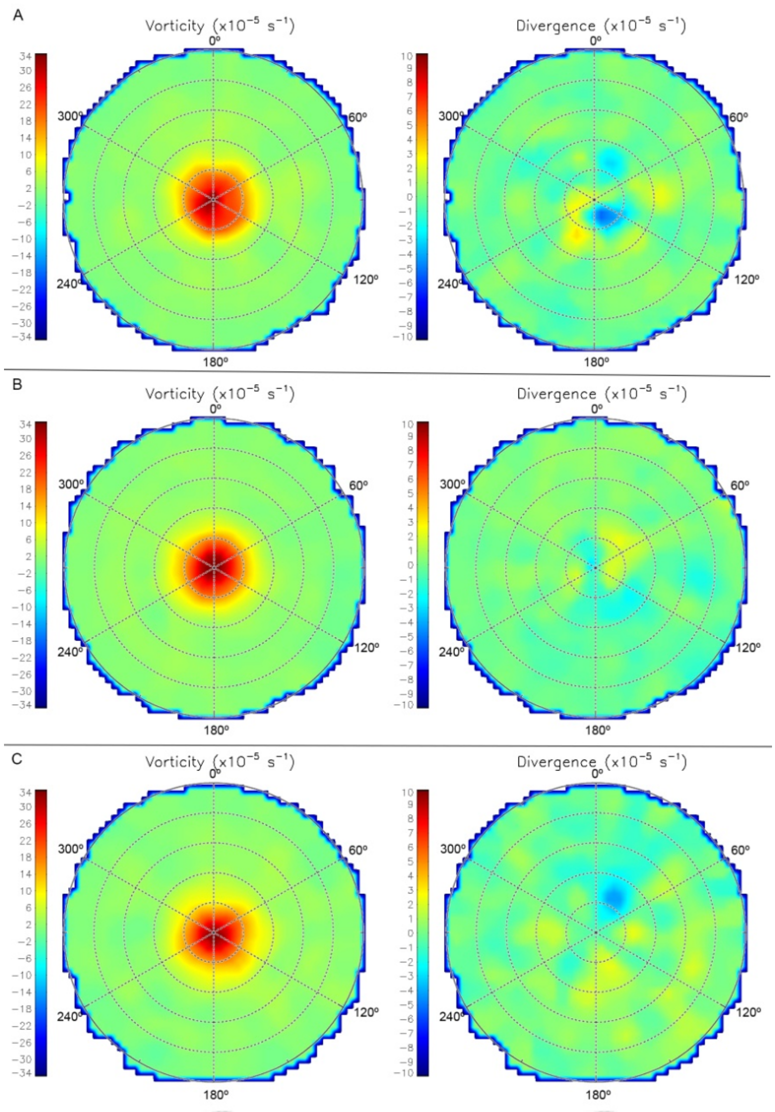

Figure 3. Relative vorticity (left) and divergence (right) maps of the north polar region between 85° and the pole for June 2013 (a), April 2014 (b) and September (2014). The dashed black circles represent the latitude between 85° and the pole every 1°. Error in those maps is ~ 4 × 10^{-5} s^{-1}, and has been estimated introducing random perturbations on the horizontal velocities.

4. Interior Region of the Hexagon

4a. Local vortices

Saturn's north and south polar regions present regular vortices of different size, shape and life-times, as observed in other latitudes (Vasavada et al., 2006; Trammell et al., 2014; Antuñano et al., 2015). For instance, at the time of Voyager flybys in 1980 and 1981 a large elliptical anticyclone of a size of ~7000-10000 km, known as the North Polar Spot (NPS) was present in the equatorial flank of the Hexagon and persisted at least until 1995 (Sánchez-Lavega et al., 1997). However, this feature was no longer present in Cassini images. Instead, a similar anticyclone was present at -66° from April 2008 to January

2009 in Cassini images, denoted as the South Polar Spot (SPS) due to its similarity with the NPS (Antuñano et al., 2015). Vortices of sizes above 3,000 km, rare in Saturn, were detected previous to Cassini orbital injection by Voyager 1 and 2 flybys at temperate subpolar latitudes of Saturn (Ingersoll et al., 1984; García-Melendo et al., 2007) and in Hubble Space Telescope images (Sánchez-Lavega et al., 2004).

In the epoch under study, we have detected at least three long-lived medium-size vortices in the region northward of the hexagon jet. An anticyclonic vortex was observed before the north polar region was illuminated by the Sun at a wavelength of 5µm in Cassini-VIMS thermal images from June 2008 at around 80.5ºN latitude (Baines et al., 2009) and it was re-observed in Cassini ISS images since January 2009 (Antuñano et al., 2015) and up to at least January 2015. The dimensions of this vortex, taking into account the outer region with lower contrasted clouds, are of 23° ± 1° (3616 ± 157 km) in longitude and 2.5° ± 0.5° (2380 ± 480 km) in latitude (see Figure 5). The peak vorticity is -7 ± 1 $x10^{-5}$ s^{-1}, approximately 1/4th of the Coriolis parameter $f = 2\Omega\, sin(\varphi)$ at that latitude, where Ω is the planetary angular velocity and φ is the latitude, and ten times the relative vorticity of the zonal winds of that region (*du/dy*). The vortex is bright when observed in methane band, and it is not observed in violet filter (VIO), suggestive of a structure with relative high cloud tops in the atmosphere. Its mean drift rate, deduced from a linear regression of the measured longitudes between November 2012 and September 2014, is $\omega =- 6.063 \pm 0.021°/\mathrm{day}$ relative to System III, which corresponds to a mean zonal velocity of $\overline{u} = 11\ \mathrm{m\,s}^{-1}$, this is, it moves in general with the background. Finally, this anticyclone migrated from higher to lower latitudes between November 2012 and January 2014, as it is shown in Figure 4.

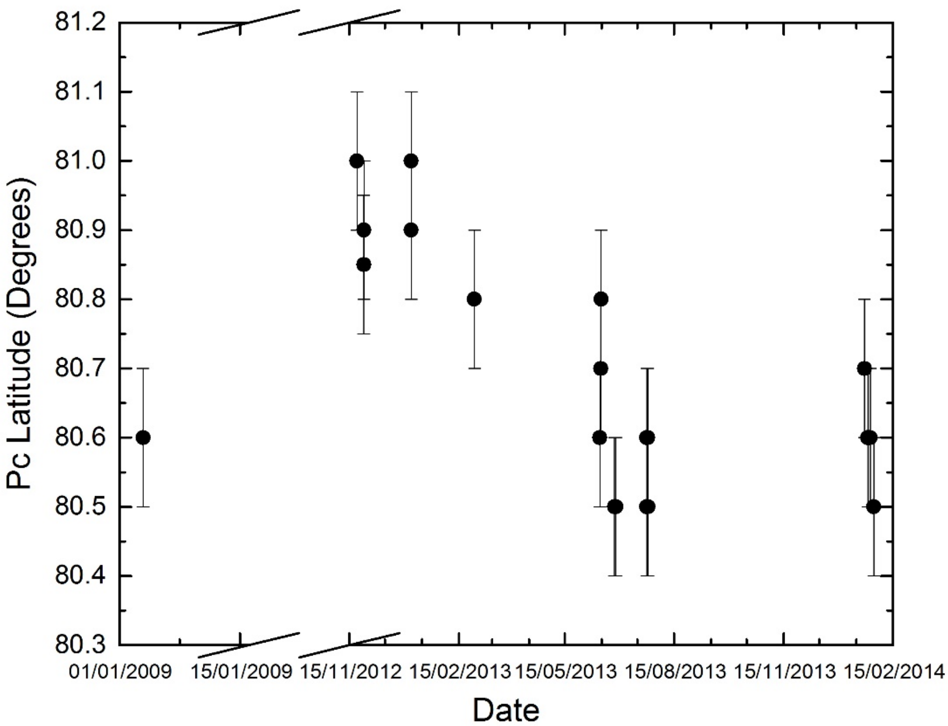

Figure 4. Latitude changes of the anticyclonic vortex at ~80.5ºN between 3 January 2009 and 29 January 2014.

Between November 2012 and November 2013, a smaller anticyclonic vortex was observed at 85.8° ± 0.1° latitude with zonal and meridional dimensions of 27° ± 3° (1879 ± 208 km) and 1.5° ± 0.1° (1425 ± 95 km) respectively. In this case, the aspect of the anticyclone in CB2 images varies significantly with time (see Figure 5). In the first images it appears elliptical and highly contrasted with an eye-like shape (dark in the center and bright in the edge, Figure 5a). Later on, the vortex became less noticeable, with a small dark part in the center surrounded by a brighter area and a dark edge (Figure 5b). Finally, by November 2013 the vortex was no longer distinguishable, maybe due to the lower resolution of the images (96 km/pixel instead of 42 km/pixel) but possibly because it was no longer present. This smaller elliptical vortex was not visible either in MT3 or VIO images. Tracking of the position of this vortex indicates that its mean zonal velocity is $\overline{u} = 96 \pm 5$ m s^{-1} (mean drift rate of $\omega = -124.0 \pm 5.6$°/day) and therefore, it moved with the background.

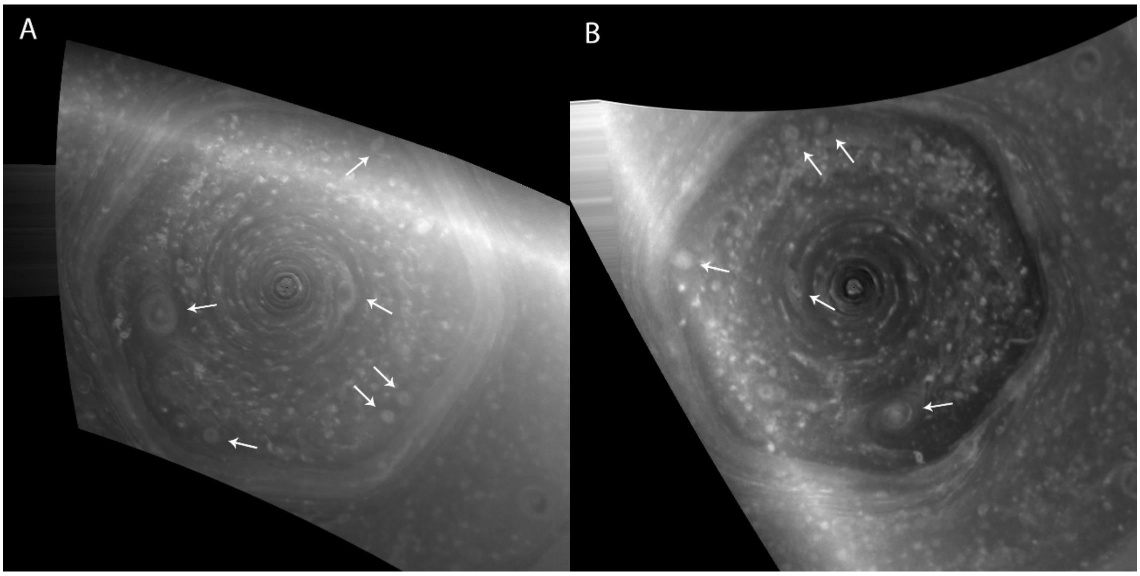

Figure 5. Two polar projections from 70° north to the pole from November 27 2012 (left) and July 23 2013 (right). The white arrows show the location of the regular closed vortices described in the text. The bright broad bands in these images are an artifact introduced by the Lambert correction applied to these polar projections in order to correct limb-darkening.

Finally, in the cyclonic shear region north of the hexagon at around 78°N latitude, smaller circular cyclonic vortices appear at different epochs in the four years, 2009-2013. Their longitudinal dimensions are 5°-7° (1000 – 1500 km) and their vorticity has been measured to be 5 ± 1 x10^{-5} s^{-1}. Over this period, between three and five vortices of this kind appear simultaneously in the latitude band 78° ± 0.5°, and all of them drifted with a mean drift rate of $\omega = -7.5 \pm 0.7$°/day, which corresponds to $\overline{u} = -17 \pm 5$ m s^{-1}, this is, they move with the local zonal wind. Some of these features can be identified in images separated by approximately four weeks indicating that their lifetime is at least one month. Identification on longer temporal intervals is inconclusive due to the lack of temporal intermediate images. We would like to point that there is a tendency towards the formation of cyclones with a size of 1000-1500 km at latitude ~78°N.

In Figure 6, we represent the zonal mean velocity of these vortices and the latitudinal location of the anticyclones and cyclones described in this section (dotted lines) and the

Hexagon and polar vortex (dashed lines) compared with the ambient zonal vorticity –*du/dy* (solid line).

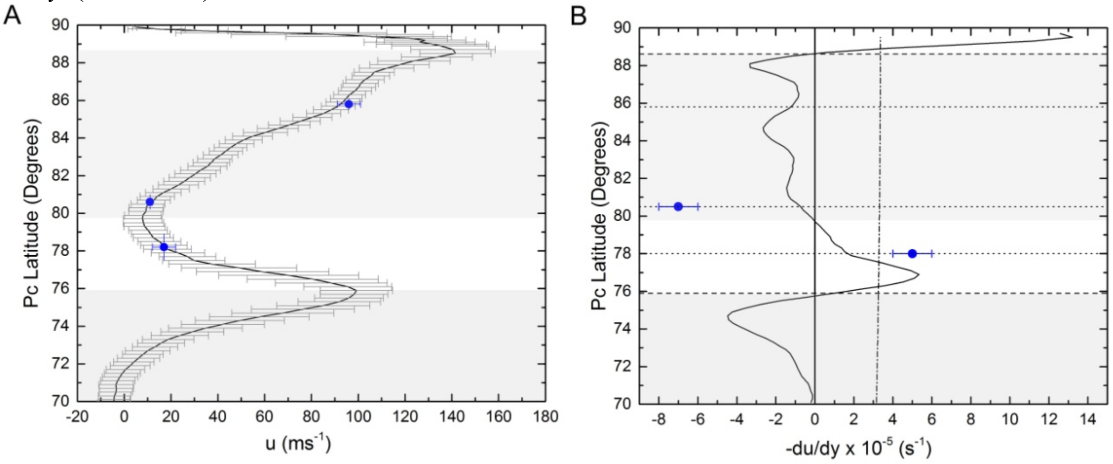

Figure 6. (A) Location and velocity of the anticyclones and cyclones (blue dots) in the zonal mean velocity profile from Antuñano et al. (2015). (B) Location and relative vorticity of the cyclones and the large anticyclone (blue dots) in the ambient flow vorticity profile (–*du/dy*) from 70ºN to the pole (solid line). The vertical dashed-dot line represents the Coriolis term. The horizontal dashed lines in panel B represent the location of the Hexagon and the polar vortex and dotted lines represent the location of the different anticyclones and cyclones described in this section. Meridional grey bands are anticyclonic areas and white bands are cyclonic areas.

The latitude of those middle size vortices showed oscillations of ~±0.5º, but they did migrate either to the pole or to the equator during the duration of our study.

4b. The "puffy" cloud field

Both Saturn's north and south polar regions exhibit a population of small compact clouds that extends from ~60°N and ~57ºS to the pole. Fields of compact clouds were observed in the south in first high-resolution images of Saturn's polar regions, and in the north in infrared images in the northern polar night (Baines et al., 2009; del Genio et al, 2009). These compact cloud fields are divided in two by the hexagonal jet in the north and the corresponding zonal jet at 70º in the south, regions where the wind shear is high.

For this study, we used a CB2 image showing the complete polar region north of the hexagon, on 25 June 2013 and a mosaic of five different CB2 images captured in a time interval of 8 hours on 3 January 2009. Figure 7 shows polar projections of the north polar region from 70° to 90° at those two dates, with a polar-projection meridional resolution of 0.01 °/pixel in the case of June 2013 and a mosaic of five polar projections with meridional resolution of 0.04 °/pixel in the case of January 2009.

Right north of the hexagon jet, a 0.5º - 0.7º meridional-wide dark and cloud-free region, is present in CB2 images following the hexagonal shape. North of this region, in the latitudinal band from 77°N to 84°N, clouds are not elongated by the wind shear. Our study concentrates in this latitudinal band. Closer to the pole, wind shear becomes important, and clouds become elongated.

The sizes of the compact clouds vary from a few tens of kilometers to one thousand kilometers and the separation between them is in the range of 150-400 km. However, the longitudinal distribution and separation of these clouds are not homogenous, and there are regions where the density of clouds is higher than in others at equivalent latitudes (see Figure 9e and f). In Figure 8 we show details of six different regions centered at different latitudes and longitudes. Panel A and B show regions centered at the same latitude with very different morphology. D and E show similar differences at a higher latitude.

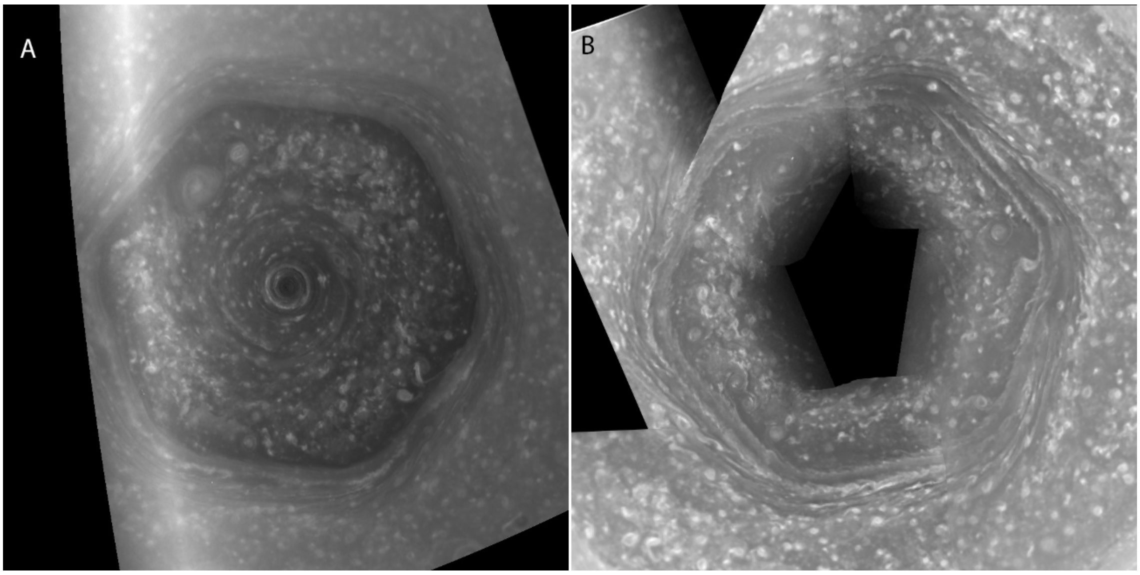

Figure 7**.** Puffy cloud field shown in a polar projection from 70º to 90º for 25 June 2013 (left) and 3 January 2009 (right). The bright broad bands in the image on the left is an artifact due to the Lambert correction applied to the polar projection.

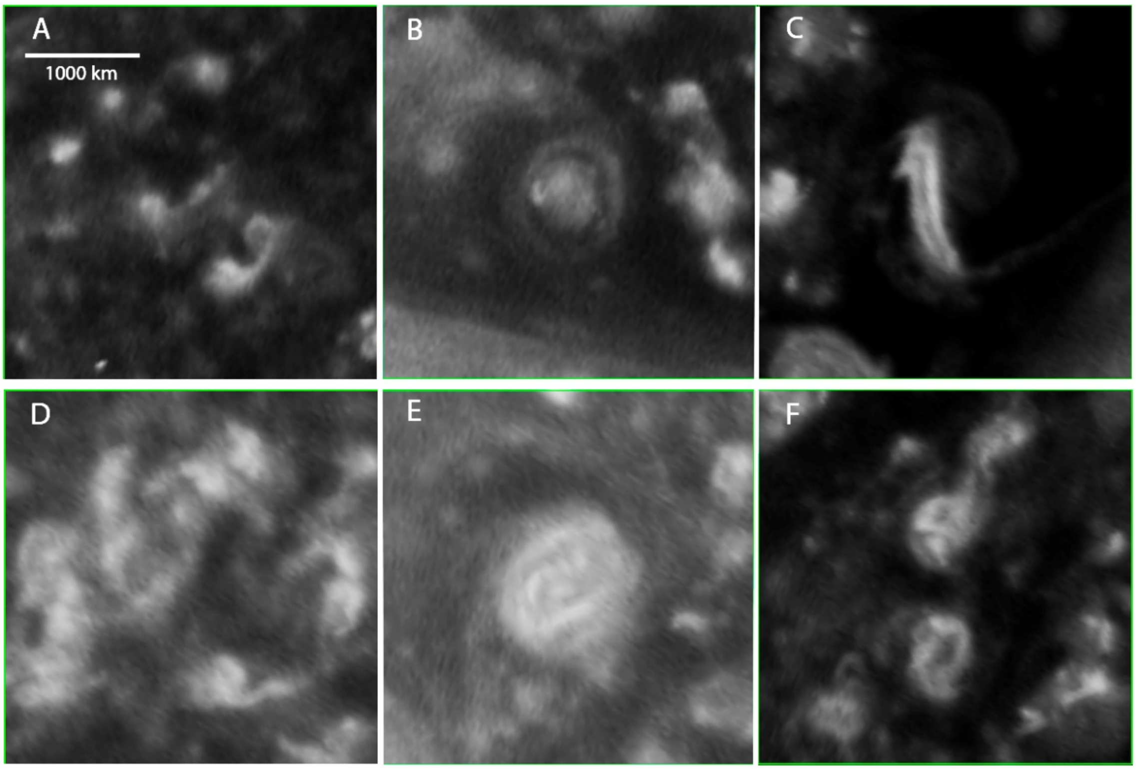

Figure 8. “Puffy” clouds in Saturn’s north polar region. These 353x353 pixels boxes of a 0.01 º/pixel meridional resolution polar projection from 25 June 2013 show the different cloud morphologies in CB2 filter found at the north polar region’s puffy cloud field. The latitude and longitude of the center of the different panels are: 78º and 165º (A), 78º and 193º (B), 79º and 122º (C), 80º and 6º (D), 80º and 341º (E) and 81º and 153º (F). The white bar represents 840 km in all the panels.

In Figure 9, we present histograms of the number of clouds against size, latitude and longitude and a plot of the mean size against latitude in two epochs, January 2009 and June 2013. The total number of clouds detected in the two epochs is 410 and 480 respectively. In the case of the distribution of sizes, the main difference between the two epochs is that in January 2009 the peak amount of clouds is found for clouds of the size of 200-300 km, while in June 2013 we find a larger number of smaller clouds of 10-200 km (a result likely due to the higher resolution of the image from June 2013). Most frequent size is of the order of the thickness of the so-called “weather” layer that encompasses the ammonia and water clouds (West et al., 2009) with a thickness of about ~ 5*H*, where *H* is the scale height ~ 50km. In the case of larger clouds, the difference in number between the two epochs is not significant. On the other hand, we find that the clouds in June 2013 are homogeneously distributed in latitude, while in January 2009 there is a significant decrease on the number of clouds in the latitudinal bands between 77º and 78º and between 82º and 84º, responsible of the lower total number of clouds detected in January 2009. However, this increase in the number of clouds might not be real as in some of the images from January 2009 the latitudinal band of 82º-84º is partially in shadow. In both epochs the maximum number of clouds per latitude bin is found around 80°N, in the minimum of the zonal wind profile.

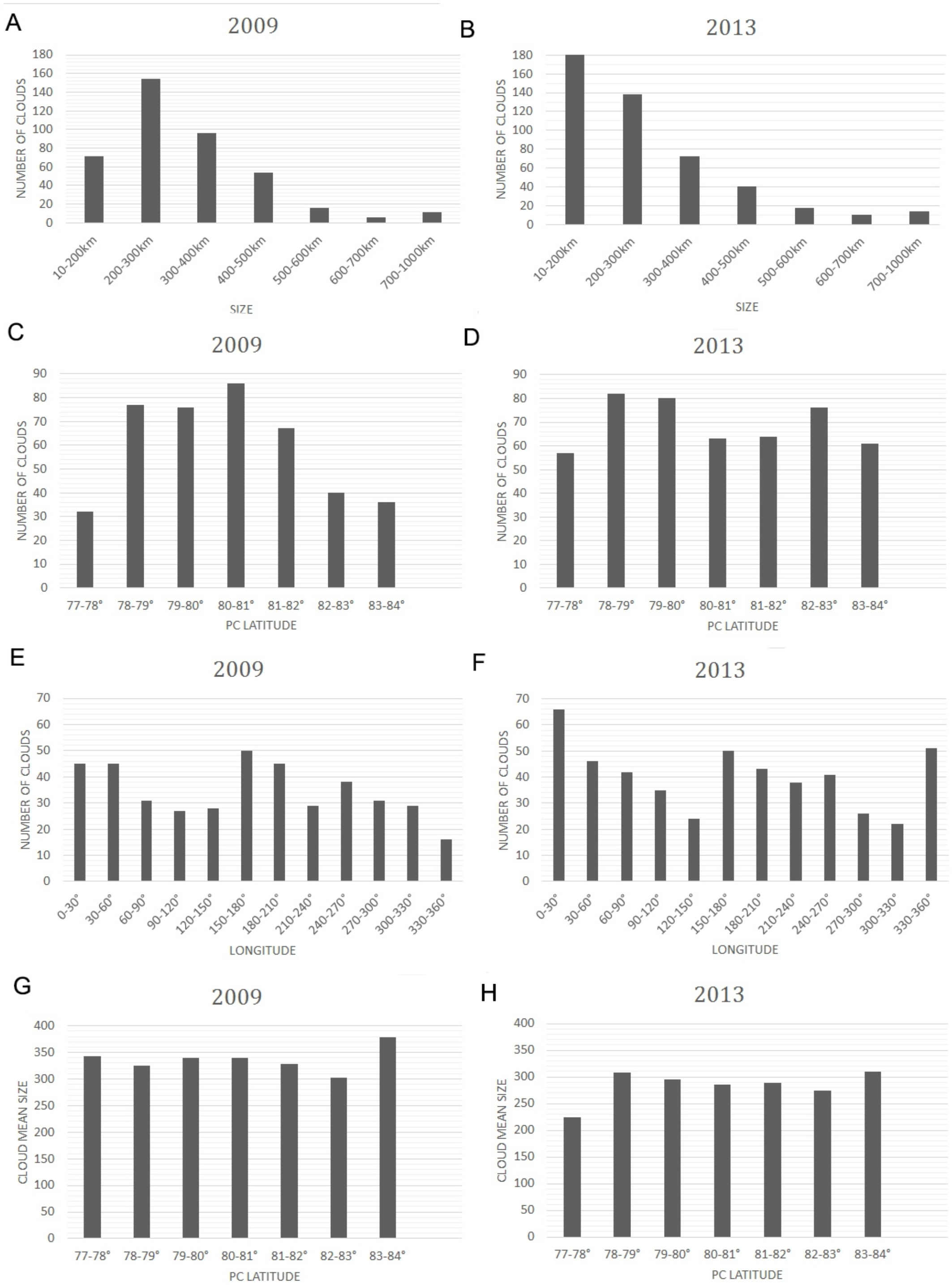

Figure 9. Statistics of the puffy cloud field for January 2009 (left) and June 2013 (right). Panels A and B show the number of clouds in different size bins, panels C and D show the latitudinal distribution of the puffy clouds, panels E and F represent the longitudinal distribution and panels G and H show the mean sizes for specific latitudinal bands. In total we detect around 410 clouds in January 2009 and 480 in June 2013.

The cloud field occurs in an ample latitudinal domain where the horizontal wind shear is low. The structure and size of the clouds resembles the groups of cumulus nimbus observed on Earth but at a much larger scale. Most of the elements show a ring-like structure, suggesting rotation and vorticity. This cloud field is probably analogous to convective cumulus cloud fields of the mesoscale cellular convection (MCC) found on

Earth and driven by the internal heat flow. Moreover, our observations tend to support the idea that the small vortices described in previous section form and grow from the merger of these features.

Interestingly, these features could be related to the formation of the polar cyclones, according to the mechanism proposed by O'Neill et al. (2015). These authors performed numerical simulations using a shallow water layer model in which forced multiple storms (plumes), emerging from moist convection, drift due to the beta effect toward the poles in the case of Saturn (not in Jupiter), where they merge and deposit their energy and cyclonic vorticity, forming the large polar vortex. This drift results from a nonlinear interaction between the small vortex and the absolute vorticity gradient (β - d^2u/d^2y). In view of the presence of the "puffy" cloud field, it seems reasonable to identify these features with the top clouds of the plumes of their model forming the small vorticity patches. Unfortunately, we were not able to measure rotation or vorticity in any of them. However, to test the above hypothesis, we tracked 24 features located between 77ºN and 85ºN during ~5 days, from 21 January 2014 to 26 January 2014. The estimated life-time of these clouds due to wind shear, $\tau_L = 1/(du/dy)$, is less than 2 days at latitudes between 78ºN and 79ºN and between 80ºN and 85ºN and less than 7-9 days at latitudes between 79ºN and 80ºN. The estimated life-time of a single element due to merger with other cloud features ranges between ~ 5 and 16 hours. Our measurements showed small oscillations in the latitude of the spots, with a mean meridional velocity for the tracked features of $\overline{v}$ =0.7±2.2 ms^{-1}, not allowing us to assess migration toward the pole. Cloud migration and merger was not detected, either, in the ring clouds delineating the north polar vortex, as reported in section 3. So, as far as our measurements permit, no evidence has been found for the mechanism proposed by O'Neill et al. (2015).

5. The Hexagon

The hexagonal feature at 75.9°N and its enclosed fast eastward jet have remained stable since the flyby of the Voyager I in 1980 (Godfrey et al., 1988; Caldwell et al., 1993; Sánchez-Lavega et al., 1993, Sánchez-Lavega et al. 2014; Antuñano et al., 2015; Sayanagi et al., 2016). The eastward jet is revealed in narrow elongated clouds of 0.3°-0.5° width, that appear in CB2 images as bright and dark filaments. High-resolution images by Cassini ISS have revealed that although the eastward jet has remained unchanged in the last 35 years, there is some transient activity inside the hexagonal jet. In particular, in 22 to 24 July 2013 and 27 November 2014, we detected two remarkable transient bright "plume-like" features in high-resolution images. These features have been indicated with an arrow in Figure 9a, corresponding to July 2013 and Figure 4a, corresponding to November 2014. A more detailed view of one of the plumes can be seen in Figure 11.

In order to analyze how these features relate to the local dynamics, we measured the zonal winds in the two epochs using (a) two image pairs from 23 July 2013 separated by 89 minutes and 125.55 minutes and (b) two image pairs from 27 November 2013 separated by 86 minutes. As mentioned above we performed wind measurements by visual cloud tracking and by a two-dimensional brightness correlation software on polar projections of 0.03 °/pixel from 70° to the pole. We sought for the position of the peak of the jet at each longitude, binning our measurements in 4 degrees longitudinal bins and 0.3 degrees latitudinal bins and calculating the maximum velocity at each longitude. Yellow arrows in Figure 10b and Figure 11b indicate the location of the velocity peak at different longitudes.

The most remarkable sign of transient activity is the plume-like feature visible in CB2 images during three days, from 22 to 24 July 2013 (see Figure 12). This feature was most noticeable in the last hours of the 23rd and first hours of the 24th, when CB2 images showed a large bright feature of maximum zonal dimension of 37.7° ± 0.5° (8746 ± 116 km) and a meridional width of 2.1° (2000 km) at the center of the feature (see Figure 10a). The head of this plume was located at 76.2° latitude, 0.9° north of the peak of velocity of the hexagonal jet at that longitude. The morphology of this feature shows an elongated dark region that divides the end of the plume longitudinally in two bright filaments. A dark region is also present close to its head. The drift of the head of this plume over this period was -33.7 ± 0.5 ^{o}/day, which corresponds to a velocity of 89 ± 1 ms^{-1}, that is, the feature moved together with the eastward jet. However, as can be seen in Figure 12, where red crosses represent the wind measurement of the small details inside the plume and the red dot represents the velocity of the head of the plume, the zonal velocity of some of the bright features of the plume differed significantly from the background motion. This signals the presence of local movements inside the hexagon and thus implies that the features are not strictly passive tracers. These details also showed a meridional velocity of ~-20 ms^{-1}, in accordance with Antuñano et al. (2015). On Cassini CB2 images from 22 July, the plume was located at a vertex of the Hexagon with a longitudinal dimension of 32 ± 1^{o} (7400 ± 232 km). The plume grew 5 ± 1^{o} in longitude in two days, reaching its maxima in the first hours of the 24th. Images taken with a violet (420 nm) and a methane band (890 nm) filters sensitive to the hazes above the main cloud layer do not show the plume (see Figure 10c and d) indicating that it is a structure trapped at cloud level.

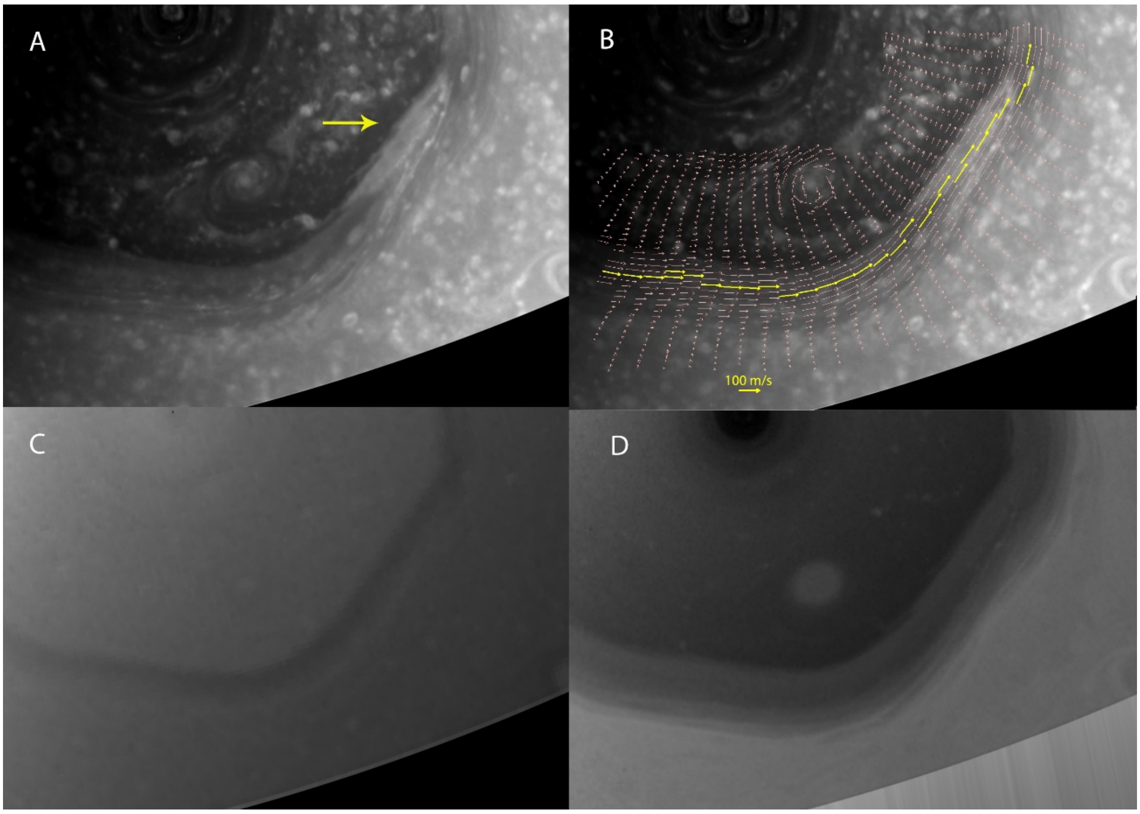

Figure 10. Four polar projections from 70°N to the pole of images from July 23 2013, in CB2 (panel A, B), violet (Panel C) and MT2 (panel D). Panel A shows the morphology of the region, including the plume-like feature (indicated by the yellow arrow) and panel B shows the wind vectors at that region. The yellow arrows indicate the position of the velocity peak at the hexagon. The data are binned in 0.3° latitude and 4° longitude bins.

On CB2 images of the 27th of November 2013 another plume-like feature was observed, this time located close to a vertex of the Hexagon, with a zonal dimension of 38° ± 1° (8400 ± 221 km) and a meridional dimension of 1.3° (1240 km) at the center of the feature, with a dark elongated region that divides the plume in two. The head of this plume was located at 76.4° latitude, 0.2° to the north of the peak of the jet at this longitude as it is shown in Figure 11b, where the yellow arrows indicate the location of the velocity peak. Its drift was -32.2 ± 0.5 °/day, which corresponds to 85 ± 1 ms^{-1}. Once again, the head of the plume moved together with the eastward jet.

On 27th of November 2013 a second transient feature was present in the hexagon region, a bright perturbed area located at 76.4° latitude of zonal dimension of 19.2° ± 1° (4345 ± 226 km) and a meridional dimension of 1.7° (1625 km) at its wider part and 1° (955 km) at its thinner part (see Figure 11a). This bright feature moved also with the velocity of the eastward jet.

Due to the lack of images of the region in the large time interval between the two mentioned epochs, we were not able to observe the formation and the entire evolution of the plumes. The elongated shape of the plumes, their brightness and the fact that they evolve in a short period (less than one month, as images from June 26 2013 do not show any plume-like feature) indicate that these features could be convective in nature. On the other hand, the expected drift of the plumes from July and November 2013, assuming they move with the jet, leads to a location of the plume in November 2013 that deviates

~100° from the expected longitude. However, we cannot conclude that these two plumes are not the same feature since a change of 5 ms^{-1} on their velocity, as it is observed, could explain the observed deviation from the expected location in the 4 months interval between the two sets of images.

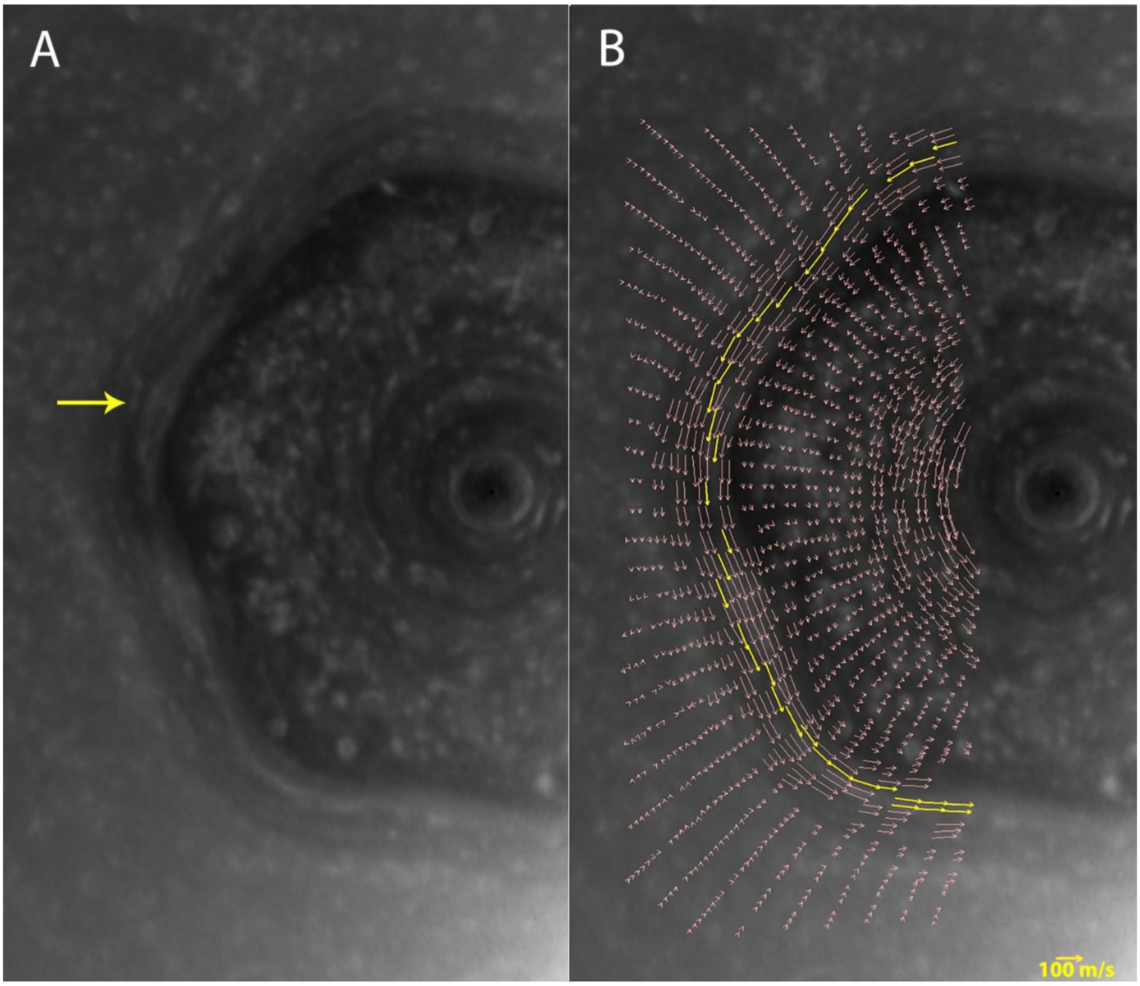

Figure 11. Two polar projections from 70°N to the pole of images from November 27 2013. Panel A shows the morphology of the region, where the yellow arrow indicates the location of the plume-like feature and panel B shows the wind vectors at that region. The yellow arrows indicate the position of the velocity peak at the hexagon. The data is binned in 0.3° latitude and 4° longitude bins.

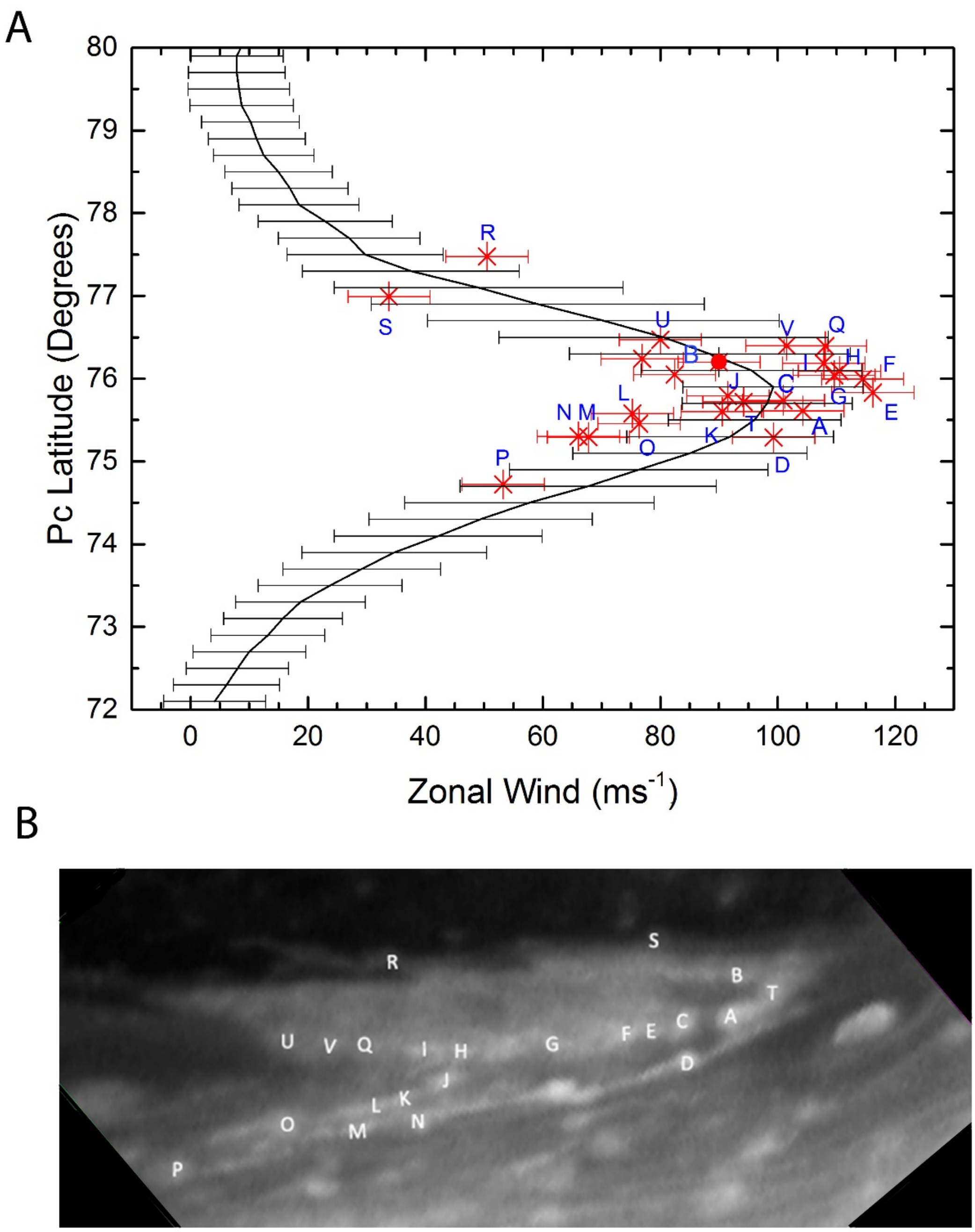

Figure 12 A) Comparison of the wind measurements of the plume head (red dot), plume features (red crosses) and the mean zonal wind profile (continuous black line) of the hexagonal eastward jet of June 2013 from Antuñano et al. (2015). B) Snapshot of a 0.02º/pixel meridional resolution polar projection centered at 76.5ºN latitude and 120.8º longitude, where the plume-like feature is clearly visible. Different letters represent the tracked features.

6. Analysis of barotropic and baroclinic instabilities to assess hexagon's origin

Different hypothesis have been proposed to explain the nature of the singular and unique hexagonal wave on Saturn: A Rossby wave forced by a large anticyclone when impinging on the jet (Allison et al., 1990), a free Rossby wave (Sánchez-Lavega et al., 2014) and a steady amplitude wavemode resulting from the finite-amplitude, nonlinear equilibration of a barotropic instability of the jet based on a laboratory fluid dynamical experiment (Barbosa-Aguiar et al., 2010). Recently, Morales-Juberías et al. (2015) performed numerical simulations using the Explicit Planetary Isentropic-Coordinate EPIC-General Circulation Model (Dowling et al., 1998) of the behavior of a zonal jet with a Gaussian shape in its meridional velocity profile centered at the latitude location of Saturn's hexagon and for the variety of parameters that define the jet. They found that the jet becomes unstable and undulates, forming a hexagonal pattern under a small perturbation to the streamfunction when the velocity has a particular vertical structure $U(y,z)$, notoriously at its base. In this model, the jet is confined at altitudes above 10-bar level and its shape violates both the Rayleigh-Kuo barotropic and the Charney-Stern baroclinic stability criterions (Sánchez-Lavega, 2011).

In this section, we explore barotropic and baroclinic stability conditions for Saturn's northern jet and its symmetric jet in the south, where no hexagon is observed (Sánchez-Lavega et al., 2002). We use a linear numerical model to obtain the growth rates of both instabilities for different tropospheric conditions using the zonal wind profiles from Antuñano et al. (2015) and the thermal profiles of Fletcher et al. (2015)

6a. Barotropic instability

In a barotropic rotating fluid the necessary, but not sufficient, condition for barotropic instability to grow is determined by the Rayleigh-Kuo criterion, which is satisfied whenever the gradient vorticity changes sign, $\beta - \frac{\partial^2 \overline{u}}{\partial y^2} < 0$, where $\beta=2\Omega\cos\varphi/R(\varphi)$ is the planetary vorticity gradient, R is the radius, u is the mean zonal flow and y is the meridional coordinate (Holton, 2004; Sánchez-Lavega, 2011). It is well known that in Saturn some of the jets, especially the eastward jets, are narrow and strong enough for the gradient of absolute vorticity to change sign at their flanks (García-Melendo et al., 2011). This condition is met for the hexagon jet and its counterpart in the south.

With the aim of studying if the hexagonal jet could be originated by this instability, we performed a linear numerical simulation assuming a barotropic flow within a β-plane approximation in a quasi-geostrophic fluid following the same procedure of Barbosa-Aguiar et al. (2010).

The barotropic vorticity equation for inviscid flows is given by (Holton, 2004; Vallis, 2006; Sánchez-Lavega, 2011)

$$\frac{Dq}{Dt} = 0 \qquad (1)$$

where $q = \nabla^2\psi + \beta y - \frac{1}{L_D^2}\psi$ is the quasi-geostrophic shallow water potential vorticity. In this expression ψ is the geostrophic stream function, β is the planetary vorticity gradient and $L_D=NH/f$ is the Rossby deformation radius, with N the Brunt-Väisälä frequency, H the height scale and f the Coriolis parameter. The advective derivative is $\frac{D}{Dt} = \frac{\partial}{\partial t} + u\frac{\partial}{\partial x} + v\frac{\partial}{\partial y}$, where the zonal and meridional wind, u and v, can be written in terms of the geostrophic stream function as $u = -\frac{\partial\psi}{\partial y}$ and $v = \frac{\partial\psi}{\partial x}$.

The vorticity deduced form the average zonal flow $\overline{u}(y)$ is a trivial solution of (1). To find a solution, we follow the standard procedure for linear small perturbations and we write the stream function as the sum of a basic state (unperturbed stream function, ψ_0) plus a small perturbation (ψ') and thus $\psi = \psi_0 + \psi'$. We seek for solutions of the form

$$\psi' = \psi'_0(y)e^{ik(x - ct)} \tag{2}$$

where $\psi'_0(y)$ is the amplitude of a small perturbation, $k = \frac{m}{R\cos(\varphi)}$ is the streamwise wavenumber, m is the zonal wavenumber, φ is the latitude of the jet, R is the planetary radius at that latitude and $c=c_r + ic_i$ is the phase speed. Instabilities will be signaled by a positive imaginary part of the phase velocity, which makes the perturbation in (2) grow exponentially.

Introducing eq. 2 into eq. 1, and ignoring second order terms, we obtain a linearized version of the quasi-geostrophic shallow-water vorticity equation:

$$(\overline{u} - c)\left\{\frac{\partial^2\psi'_0}{\partial^2 y} - k^2\psi'_0\right\} + \left\{\beta - \frac{\partial^2\overline{u}}{\partial^2 y} - \frac{1}{L_D^2}\right\}\psi'_0 = 0, \tag{3}$$

We solved this problem over a latitudinal range of -5000 km ≤ y ≤ 5000 km using the Gaussian approximation of the zonal mean profile

$$u = u_0 e^{-bR^2(y - y_0)^2/2u_0} \tag{4}$$

with the measured parameters taken from Antuñano et al. (2015); for the hexagonal jet b = 8.0x10^{-11} m^{-1} s^{-1} and u_0=104 m s^{-1} and for its counterpart in the south b = 5.0x10^{-11} m^{-1} s^{-1} and u_0= 88 m s^{-1}.

Following Barbosa-Aguiar et al. (2010), we used Neumann boundary conditions $\frac{\partial\psi'_0}{\partial y} = 0$ at the upper and lower latitudes. However, we have checked that for the narrow jets under study the use of Dirichlet boundary conditions (ψ'_0=0) or mixed boundary conditions leads to identical results. Once boundary conditions are imposed, the problem becomes an eigenvalue problem that we solve approximating the derivatives with the Finite Difference Method (FDM).

In Figure 13, we present the results of this eigenvalue problem, showing the growth rate curves (kc_i) for different zonal wavenumbers (m) and for different values of the Rossby deformation radius (L_D= NH/f). For the Hexagon jet a maximum zonal wavenumber of m=6 with an e-folding time scale of ~14 T_s (Saturnian days) is obtained for a Rossby deformation radius of L_D=1000 km, that is, assuming a scale height H ~ 50 km, corresponds to a Brunt-Väisälä frecuency of N^2 = 4x10^{-5} s^{-2}, both typical values of Saturn's upper troposphere (we take the data from Sánchez-Lavega, 2011, and references therein). For the counterpart eastward jet at 70.4ºS the results show a maximum zonal wavenumber of m = 7 with ~28T_s for a Rossby deformation radius of L_D=1000 km or a maximum zonal wavenumber of m=9 and e-folding time scale of ~28 T_s for L_D=1500 km.

The fact that images from the south polar region do not show any wave pattern at the eastward jet at 70.4ºS (Sánchez-Lavega et al., 2004), is not in contradiction with our results as this kind of analysis does not provide information about the equilibration amplitude of the perturbation, which could be small enough at the jet in the south to hide any wave-like pattern.

These results differ from the growth-rate curves presented by Barbosa-Aguiar et al. (2009), where they obtained m=6 for the hexagonal jet for a value of the deformation ratio 2.5 times larger, leading to an e-folding time around 7 times larger than our results. Moreover, in the case of the jet at 70.4ºS, their growth-rate analysis does not show any finite wavenumber. These differences may be due to the fact that in our model we used improved zonal profiles.

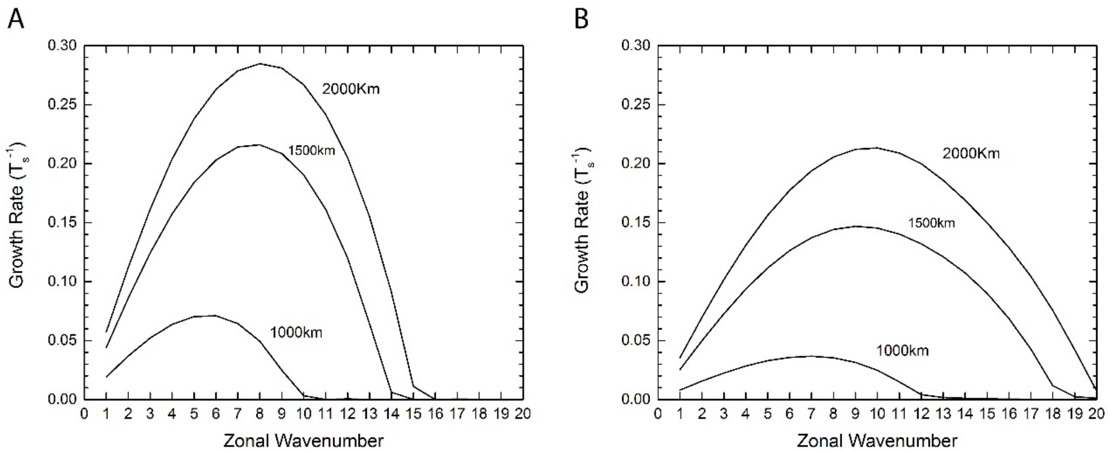

Figure 13. Growth rates of the barotropic instability for jet profile within the hexagon (A) and its jet counterpart in the south (B) for different Rossby deformation radius. Growth rate curves are given in T_s^{-1}, where T_s is a Saturnian day.

6b. Baroclinic instability

As in the previous section, we performed a linear numerical simulation within the β-plane approximation under quasi-geostrophic conditions for the hexagonal jet and its counterpart in the south, this time considering a baroclinic jet. We follow the formalism of Godfrey and Moore (1986) in their exploration of instability of Saturn's "ribbon" wave. Again, we solve equation (1) but with the quasi-geostrophic potential vorticity defined as $q = \nabla^2\psi + \beta y + \frac{\partial}{\partial z}\left(\frac{f^2 \partial\psi}{N^2 \partial z}\right)$, where ψ is the geostrophic stream function that takes into account the altitude dependences in the third term.

In order to linearize the vorticity equation, we assume small perturbations of the eddy stream function and we write again the stream function as the sum of a basic state plus a small perturbation $\psi = \psi_0 + \psi'$. We look for solutions periodic in time and in the horizontal and meridional directions, *x* and *y*, that is

$$\psi' = \psi'_0(z)e^{\left(i\left(k_x(x - ct) + k_y y\right)\right)} \quad (5)$$

where k_x and k_y are the zonal and meridional wavenumbers and $c=c_r + ic_i$ is once again the phase speed and the eigenvalue of this problem. We solve the problem in a region limited at the top at $P = 100$ mbar (tropopause) and we consider different altitude locations of the bottom layer. Following Godfrey and Moore (1986), we impose a rigid top as boundary condition at the upper layer, which implies that

$$(\bar{u} - c)\frac{\partial \psi'_0}{\partial z} - \frac{\partial \bar{u}}{\partial z}\psi'_0 = 0 \quad (6)$$

at P = 100 mbar (tropopause), and Dirichlet boundary condition ψ'_0=0 at the bottom layer.

Introducing eq. 5 into eq. 1, and ignoring second order terms, we obtained the linearized quasi-geostrophic vorticity equation (Godfrey and Moore, 1986):

$$(\bar{u} - c)\left[\frac{f^2}{\rho}\frac{\partial}{\partial z}\left(\frac{\rho}{N^2}\frac{\partial \psi'_0}{\partial z}\right) - \left(k_x^2 + k_y^2\right)\psi'_0\right] + \left[\beta - \frac{\partial^2 \bar{u}}{\partial^2 y} - \frac{f^2}{\rho}\frac{\partial}{\partial z}\left(\frac{\rho}{N^2}\frac{\partial \bar{u}}{\partial z}\right)\right]\psi'_0 = 0, \quad (7)$$

where $\bar{u}$ is the peak velocity of the jet under study. To solve this eigenvalue problem we use realistic measured values for the parameters of the jet taken from Antuñano et al. (2015): $\bar{u}$=104 ms^{-1}, $\bar{u}_{yy}$=-0.6x10^{-10} m^{-1}s^{-1}, f = 3.2x10^{-4} s^{-1}, β = 1.4x10^{-12} m^{-1}s^{-1} for the hexagon and $\bar{u}$=88 ms^{-1}, $\bar{u}_{yy}$=-0.5x10^{-10} m^{-1}s^{-1}, f = -3.1x10^{-4} s^{-1}and β=2x10^{-12} m^{-1}s^{-1} for the eastward jet at 70ºS. In both cases we used k_y=0, as this gives rise to the maximum growth rate. The Brunt-Väisälä frequency is now a function of the altitude and is defined as the square root of

$$N^2(z) = \frac{g}{T}\left(\frac{dT}{dz} + \frac{g}{C_p}\right), \quad (9)$$

(Sánchez-Lavega, 2011) where $g \sim 9.5$ ms^{-2} is the gravity at the studied latitude, T is the temperature, z is the height relative to P_0 = 700 mbar (the assumed location of the cloud tops where the zonal winds have been measured), and C_p is the normal specific heat. We have used the temperature profiles at 75ºN and 70ºS retrieved by Fletcher et al. (2015), which cover depths from 100 mbar to 1 bar for June 2013 in the north and December 2008 in the south. The temperature profiles, $T(z)$, and $N^2(z)$ are represented in Figure 14.

In a baroclinic problem, the static stability must be positive everywhere, and this implies that $N^2 > 0$. However, when the retrieved profiles of Fletcher et al. (2015) are introduced in equation (9) N^2 at the latitude of the hexagon changes sign at around 350 mbar, becoming negative, as can be seen in Figure 14c. In order to regularize this situation we considered a constant small positive N^2 bellow this pressure level. This value is chosen taking into account that the temperature grows adiabatically below ~500 mbar (N^2=0) and that the Richardson number, $Ri = N^2/(\partial u/\partial z)^2$, it is typically between ~ 1 and 1000 for a baroclinic instability to develop (Holton, 2004; Sánchez.Lavega, 2011). We used N^2=0.17x10^{-5} s^{-1} (Ri=170) for the hexagon jet at pressures bellow 350 mbar (see Figure 14e). In the case of the eastward jet in the south, the retrieved temperature profile does not lead to negative values of the static stability, and we took the lowest value of the

Brunt-Väisälä frequency, N^2=0.3x10^{-5} s^{-1} (R_i=300), as a constant value for pressures below 600 mbar (see Figure 14f).

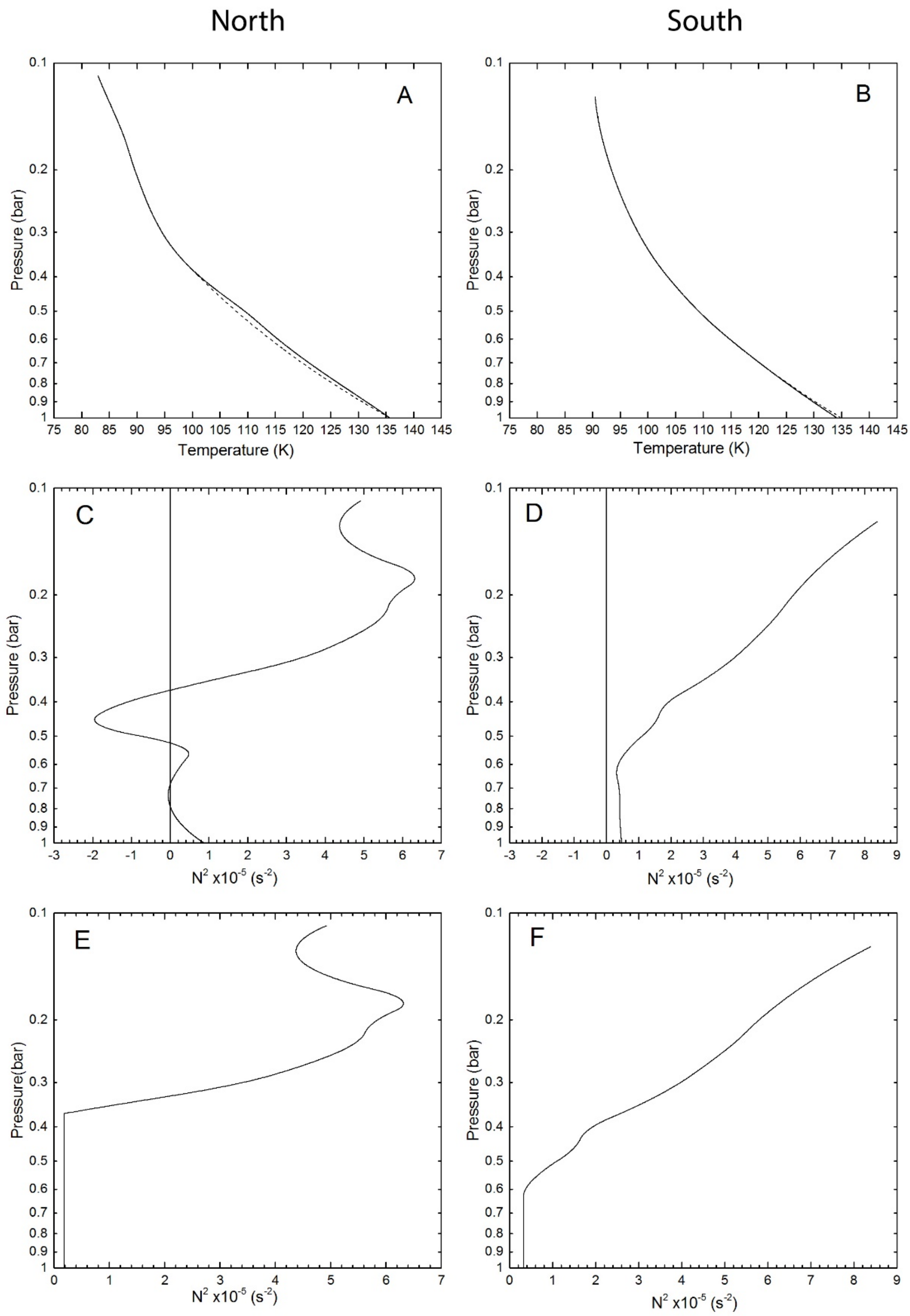

Figure 14. Solid line in Panels A and B represent respectively the temperature profile at 75ºN from June 2013 and at 70ºS from December 2008 (Fletcher et al. 2015). Panels C

and D represent the Brünt-Väisälä frequency for the Hexagon and its counterpart deduced from these temperature profiles. Panels E and F represent the regularized Brünt-Väisälä frequency used in our calculation, for the Hexagon and the eastward jet in the south, respectively. Finally, dashed lines in panel A and B represent the temperature profiles consistent with the regularized Brünt-Väisälä frequency, used in our calculation.

Finally, we use a vertical wind shear $du/dz = -0.1\ ms^{-1}/km$, for both north and south, which is a mean value obtained from the meridional temperature gradient at different pressure levels using the thermal wind equation and the data from Fletcher et al. (2015).

We have calculated growth rates for five different depths of the bottom layer (1 bar to 5 bar) using the N^2 profiles presented in Figure 14e and Figure 14f. Within this frame our results, shown in Figure 15, indicate that the growth rate peaks at large zonal wave numbers, both at the latitude of the hexagon (m~30-35) and its counterpart in the south (m~25-30), considerably different to what we see in the hexagon.

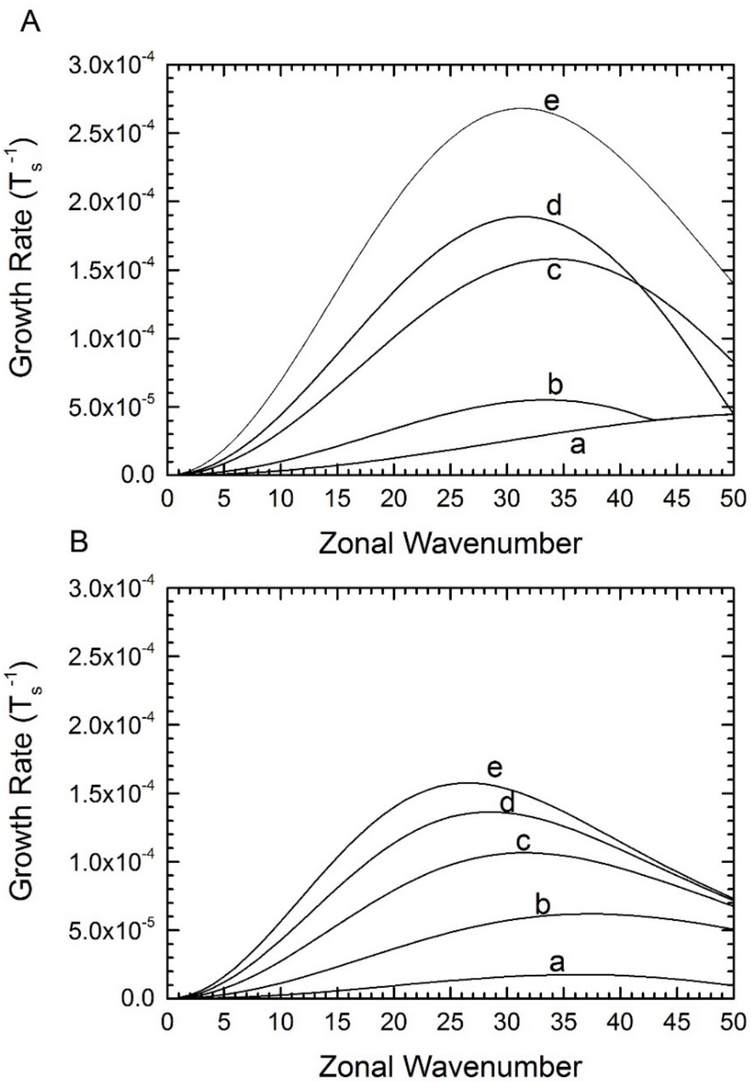

Figure 15. Growth rates of the studied 1D baroclinic instability for the hexagon jet (A) and its counterpart in the south (B). Different curves represent how the growth rate changes when the lower boundary changes from 1 bar (a) to 5 bars (e).

In this study, we use a vertical temperature profile with dT/dz ranging between -0.37 K/km and -0.9 K/km, in agreement with the values used in Morales-Juberías et al. (2015).We use a simpler *du/dz* profile, which we assume equal to -0.1m s^{-1}/km at the region under study, while Morales-Juberías et al. (2015) use an altitude dependent vertical wind-shear ranging between -0.5 m s^{-1}/km and -0.1 m s^{-1}/km. Our fastest growing modes differ from the results of Morales-Juberías et al. (2015), but it must be taken into account that we present a simple baroclinic model that explores the fastest growing modes of the instability according only to reasonable vertical profiles of the wind speed and temperature. A thorough exploration that takes into consideration the meridional dependence of the wind profile is part of an ongoing study.

7. Conclusions

In this paper, we have presented a study based on Cassini ISS images of the cloud morphology and dynamics of Saturn's north polar region encompassing the latitudes from the Hexagon at 76ºN to the pole. The period covered was from January 2009 to November 2014. Our main conclusions are:

- **Hexagon:** The meandering hexagonal jet at 75.9ºN has remained unchanged over decades, but shows different episodes of activity characterized by bright plume-like features with zonal dimensions of 8650 ± 120 km. A conspicuous plume in July 2013 showed some local movement inside the Hexagon jet as the velocity of some of the bright details inside the plume differed from background motions. However, the head of the plume moved with the jet speed. Due to its brightness, its elongated shape and its rapid evolution, it is likely that this plume-like feature is of convective nature. In any case, there are no signs of the feature in the upper haze layer and of a different velocity relative to the ambient flow.

- **North Polar Vortex:** The cloud morphology and albedo changed between November 2012 and September 2014 in the rings of clouds that delineate the vortex circulation. No changes where observed in the vortex wind field, vorticity and divergence.

- **Vortices in the polar area:** We observed and tracked different anticyclones and cyclones over four-year interval, 2009-2013. The cyclones are circular in shape with diameters of 1000-1500 km and located at 78° ± 0.5° planetocentric latitude. They are transient features with a life-time of at least one month. These vortices, and two other large anticyclones present at 80.5° and at 85.8° latitude with life-times of at least seven years and one year, respectively, showed small oscillations of ~±0.5° in latitude. However, they did not show measurable migration to the poles or equator over the studied time interval.

- **Puffy cloud field:** A field of what we call "puffy clouds" is permanently present from 60ºN to the pole. In the region from 77ºN to 84ºN, most clouds in the field had sizes from a few tens of km to 300 km, and just a few of them were larger than 500 km, both in January 2009 and in June 2013. These “puffy clouds” sometimes had a ring like structure that denotes the presence of vorticity. The number of clouds per latitudinal area is overall homogeneous at both epochs. However, the longitudinal distribution was not homogeneous in any of the two studied epochs (January 2009 and June 2013). Thus, the results did not show any correlation between seasonal changes in Saturn’s North Polar egion and changes in the sizes and number of the puffy clouds. The life-time of the small clouds, due to wind shear, is less than 9 days. Again, we did not detect meridional migrating motions of these compact clouds

- **Barotropic and Baroclinic instability**: We explore the growing modes for an unstable barotropic or baroclinic jet. We solve the linearized quasigeotrophic equation within the β-plane approximation, using as input realistic parameters retrieved from the literature. The results show that the growth rates of the barotropic instability in a shallow water approximation occur for a Rossby deformation length L_D=1000 km and have a maximum at wavenumber 6 for the hexagonal jet and at wavenumber 7 for the jet at 70.4ºS. This is in accordance with the observations for the hexagon. Nevertheless, there is no equivalent wave-like instability in the south. On the other hand, the results of our baroclinic one-dimmensional analysis show that for realistic values of N^2 and d*u*/d*z* and for all considered bottom layer depths, the wavenumber of the maximum growth rate is ~ 30-35, much larger than 6.

The ongoing observations made by the Cassini spacecraft until its Grand Finale in September 2017 will allow completing the study of the evolution of all the dynamical formations present in the North Polar Region. Particularly relevant for these studies will be the determination of the internal structure of the planet from the measurements of the gravitational field and the determination of its real rotation period in order to fix the intensity of the winds (Sánchez-Lavega, 2005).

With these new and critical data it will be possible to formulate much more advanced dynamic models of the polar regions.

Acknowledgements

This work was supported by the Spanish MICIIN projects AYA2015-65041 with FEDER support, Grupos Gobierno Vasco IT-765-13, and UFI11/55 from UPV/EHU.

References

Allison, M., Godfrey, D. A. and Beebe, R. F., 1990. A wave dynamical interpretation of Saturn’s Polar Hexagon. Science, 247, 1061–1063.

Antuñano, A., del Río-Gaztelurrutia, T., Sánchez-Lavega, A. and Hueso, R., 2015. Dynamics of Saturn’s polar regions. J. Geophys. Res. Planets, 120, 155-176.

Baines, K.H., Momary, T.W., Fletcher, L.N., Showman, A.P., Roos-Serote, M., Brown, R. H., Buratti, B.J., Clark, R.N. and Nicholson, P.D., 2009. Saturn’s north polar cyclone and hexagon at depth revealed by Cassini/VIMS. Planetary and Space Science, 57, 1671-1681.

Barbosa Aguiar, A.C., Read, P.L., Wordsworth, R.D., Salter, T. and Yamazaki, Y.H., 2010. A laboratory model of Saturn's North Polar Hexagon. Icarus, 20**6**, 755-763.

Caldwell, J., Hua, X-M., Turgeon, B., Westphal, J.A. and Barnet, C.D., 1993. The drift of Saturn's North Polar Spot by the Hubble Space Telescope. Science, 260, 326-329.

Desch M. D., Kaiser, L. M., 1981. Voyager measurements of the rotation period of Saturn's magnetic field. Geophys. Res. Lett., 8, 253-256.

Del Genio, A.D., Achterberg, R.K., Baines, K.H., Flasar, F.M., Read, P.L., Sánchez-Lavega, A. and Showman, A.P., 2009. Saturn Atmospheric Structure and Dynamics. Chaper 6 in: Saturn after Cassini-Huygens. M. Dougherty, L. Esposito and T. Krimigis (edt.), Springer-Verlag, 113-159.

Dowling, T.E., Fischer, A.S., Gierasch, P.J., Harrington, J., LeBeau, R.P. Jr. and Santori, C.M., 1998. The explicit planetary isentropic-coordinate (EPIC) atmospheric model. Icarus, 132, 221-238.

Dyudina, U.A., Ingersoll, A.P., Ewald S.P., Vasavada, A.R., West, R.A., Del Genio, A.D., Barbara, J.M., Porco, C.C., Achterberg, R.K., Flasar, F.M., Simon-Miller, A.A. and Fletcher, L.N., 2008. Dynamics of Saturn's South Polar Vortex. Science, 319, 1801.

Dyudina, U.A., Ingersoll, A.P., Ewald, S.P., Vasavada, A.R., West, R.A., Baines, K.H., Momary, T.W., Del Genio, A.D., Barbara, J.M., Porco, C.C., Achterbebrg, R.K., Flasar, F. M., Simon-Miller, A.A. and Fletcher, L.N., 2009. Saturn's south polar vortex compared to other large vortices in the Solar System. Icarus, 202, 240-248.

Fletcher, L.N., Irwin, P.G.J., Orton, G.S., Teanby, N.A., Achterberg, R.K., Bjoraker, G.L., Read, P.L., Simon-Miller, A.A., Howett, C., de Kok, R., Bowles, N., Calcutt, S.B., Hesman, B. and Flasar, F.M., 2008. Temperature and composition of Saturn's polar hot spots and hexagon. Science, 319, 79-81.

Fletcher, L.N., Irwin, P.G.J., Sincalir, J.A., Orton, G.S., Giles, R.S., Hurley, J., Gorius, N., Achterberg, R.K., Hesman, B.E. and Bjoraker, G.L., 2015. Seasonal evolution of Saturn's polar temperatures and composition. Icarus, 250, 131-153.

García-Melendo, E., Sánchez-Lavega, A. and Hueso, R., 2007. Numerical models of Saturn's long-lived anticyclones. Icarus, 191**,** 665-677.

García-Melendo, E., Pérez-Hoyos, S., Sánchez-Lavega and Hueso, R., 2011. Saturn's zonal wind profile in 2004-2009 from Cassini ISS images and its long-term variability. Icarus, 2015, 62-74.

Godfrey, D. A., 1988. A hexagonal feature around Saturn's north pole. Icarus, 76, 335–356.

Godfrey, D.A. and Moore, V., 1986. The Saturnian Ribbon feature-A baroclinic unstable model. Icarus, 68, 313-343.

Holton, J.R., 2004. An Introduction to Dynamic Meteorology. Elsevier Academic Press.

Hueso, R., Legarreta, J., Rojas, J.F., Pérez-Hoyos, S., del Río-Gaztelurrutia, T. and Sánchez-Lavega, A., 2010. The Planetary Laboratory for Image Analysis (PLIA). Adv. Space Res., 6, 1120-1138.

Hueso, R., Legarreta, J., García-Melendo, E., Sánchez-Lavega, A. and Pérez-Hoyos, S., 2009. The Jovian anticyclone BA: II. Circulation and models of its interaction with the zonal jets. Icarus, 203, 499–515.

Hunt, G. E. and Moore, P., 1982. "Saturn". Rand-McNally, London

Ingersoll, A.P., Beebe, R. F., Conrath, B.J., Hunt, G.E., 1984. Structure and dynamics of Saturn's atmosphere, in *Saturn,* T. Gehrels and M. S. Matthews (eds.), University of Arizona press, Tucson, 195 – 238.

Mitchell, D.M., Montabone, L., Thomson, S. and Read, P.L., 2014. Polar vortices on Earth and Mars: A comparative study of the climatology and variability from reanalyses. G. J. R. Meteorol. Soc, 141, 550-562.

Morales-Juberías, R., Sayanagi, K.M., Simon, A.A., Fletcher, L.N. and Cosentino, R.G., 2015. Meandering shallow atmospheric jet as a model of Saturn's north-polar hexagon. Astrophys. J. Lett., 8016, L18.

O'Neill, M.O., Emanuel K.A. and Flierl, G.R., 2015. Polar vortex formation in giant-planet atmospheres due to moist convection. Nature Geoscience, 8, 523-526.

Orton, G.S. and Yanamandra-Fisher, P.A., 2005. Saturn's Temperature Field from High-Resolution Middle-Infrared Imaging. Science, 307, 696-698.

Porco, C.C. et al., 2004. Cassini imaging science: Instrument characteristics and anticipated scientific investigations at Saturn. Space Sci. Rev., 115, 363–497.

Sánchez-Lavega, A., Lecacheux, J., Colas, F. and Laques, P., 1993. Ground-Based observations of Saturn's North Polar Spot and Hexagon. Science, 260, 329-332.

Sánchez Lavega A., Rojas, J. F., Acarreta, J. R., Lecacheux, J., Colas, F. and Sada, P. V., 1997. New Observations and studies of Saturn's long-lived North Polar Spot. Icarus, 128, 322-334.

Sánchez-Lavega, A., Pérez-Hoyos, S., Acarreta, J.R. and French. R., 2002. No hexagonal wave around Saturn's southern pole. Icarus**,** 160, 216 - 219 .

Sánchez-Lavega, A., Hueso, R., Pérez-Hoyos, S., Rojas, J.F. and French, R.G., 2004. Saturn's Cloud Morphology and Zonal Winds Before the Cassini Encounter. Icarus, 170, 519-523.

A. Sánchez-Lavega. 2005. "How long is the day on Saturn?", Science, 307, 1223-1224.

Sánchez-Lavega, A., Hueso, R., Pérez-Hoyos, S. and Rojas, J. F., 2006. A strong vortex in Saturn's south pole. Icarus, 184, 524-531.

Sánchez-Lavega, A, 2011. An Introduction to Planetary Atmospheres, Taylor-Francis, CRC Press Boca Raton, Florida.

Sánchez-Lavega, A., del Río-Gaztelurrutia, T., Hueso, R., Pérez-Hoyos, S., García-Melendo, E., Antuñano, A., Mendikoa, I., Rojas, J. F., Lillo, J., Barrado-Navascués, D., Gomez-Forrellad, J. M., Go, C., Peach, D., Barry, T., Milika, D. P., Nicholas, P. and Wesley, A., 2014. The long-term steady motion of Saturn's hexagon amd the stability of its enclosed jet stream under seasonal changes. Geophysical Reseach Letters, 41, 1425-1431.

Sayanagi, K.M., Ewald, S. P., Dyudina, U. A. and Ingersoll, A. P., 2013. American Astronomical Society. DPS meeting #45, #509.06. 10.

Sayanagi, K.M., Baines, K.H., Dyudina, U.A., Fletcher, L.N., Sánchez-Lavega, A. and West, R.A., 2016. Saturn's Polar Atmosphere. ArXiv, Astro-Ph.EP: 1609.09626v2.

Sayanagi, K.M., Blalock, J.J., Dyudina, U.A., Ewald, S.P. and Ingersoll, A.P., 2017. Cassini ISS observation of Saturn's north polar vortex and comparison to the south polar vortex. Icarus, 2805, 68-82.

Seidelmann, P. K., Archinal, B. A., A'Hearn, M. F., Conrad, A., Consolmagno, G. J., Hestroffer, D., Hilton, J. L., Krasinsky, G. A., Neumann, G., Oberst, J., Stooke, P., Tedesco, E. F., Tholen, D. J., Thomas, P. C. and Williams, I. P., 2007. Report of the IAU/IAG working group on cartographic coordinates and rotational elements: 2006. Celestial Mech. Dyn. Astron. 98, 155-180.

Snyder, J. P., 1987. Map Projections-A Working Manual. U. S. Geological Survey Professional Paper 1395. Washington, DC: U. S. Government Printing Office, 191-202.

Trammell, H.J., Li, L., Jiang, X., Smith, M., Hörst, S. and Vasavada, A., 2014. The global vortex analysis of Jupiter and Saturn based on Cassini Imaging Science Subsystem. Icarus, 242, 122-129.

Vallis, G.K., 2006. Atmospheric and Oceanic Fluid Dynamics. Cambridge University Press.

Vasavada, A.W., Hörst, S.M., Kennedy, M.R., Ingersoll, A.P., Porco, C.C., Del Genio, A.D., West, R.A., 2006. Cassini imaging of Saturn: Southern hemisphere winds and vortices. Journal of Geophysical Research, 111, E05004.

West, R.A., Baines, K.H., Karkoschka, E. and Sánchez-Lavega, A., 2009. Saturn after Cassini-Huygens. Springer, Ch. 7, pp. 161-179.

APPENDIX

Table1: Images form Cassini ISS used for this study.

Cassini Orbiter ISS volume	Image ID	Date	Time	Camera Filter	Resolution (Subspacecraft) (km/pixel)	Subsolar latitude (º)	Subspacecraft latitude (º)	Phase angle (º)
2052	W1609672855_1	03/01/2009	10:41:01	CB2	83.7	-3	69	80
2052	W1609678135_1	03/01/2009	12:09:01	CB2	83.0	-3	69	82
2052	W1609686055_1	03/01/2009	14:21:01	CB2	80.5	-3	69	86
2052	W1609693975_1	03/01/2009	16:33:01	CB2	78.1	-3	68	91
2052	W1609699455_1	03/01/2009	18:04:21	CB2	76.4	-3	67	94
2078	W1732683971_1	27/11/2012	04:12:32	CB2	21.6	16	39	93
2078	N1732691412_1	27/11/2012	06:16:32	BL2	2.2	16	43	81

2078	N1732691474_1	27/11/2012	06:17:34	GRN	4.5	16	43	81
2078	N1732691523_1	27/11/2012	06:18:23	UV3	4.5	16	43	81
2078	W1732692878_1	27/11/2012	06:40:58	CB2	24.5	16	44	79
2078	W1732701785_1	27/11/2012	09:09:25	CB2	23.9	16	46	66
2080	W1736125656_1	06/01/2013	00:13:35	CB2	106.5	17	53	66
2080	W1736133454_1	06/01/2013	02:23:33	CB2	112.5	17	52	57
2081	W1740620364_1	28/02/2013	00:44:54	CB2	35.7	17	49	40
2083	W1749823807_1	13/06/2013	13:14:39	CB2	68.6	19	50	94
2083	N1749893078_1	14/06/2013	08:29:09	RED	4.2	19	53	46
2083	N1749893118_1	14/06/2013	08:29:49	BL2	8.4	19	53	46
2083	N1749893150_1	14/06/2013	08:30:21	UV3	8.4	19	53	46
2083	N1749893313_1	14/06/2013	08:33:04	GRN	4.2	19	53	46
2083	N1749893434_1	14/06/2013	08:35:05	MT2	4.2	19	53	46
2083	N1749893515_1	14/06/2013	08:36:22	CB2	4.2	19	53	46
2083	W1749911278_1	14/06/2013	13:32:29	CB2	4.5	19	47	36
2083	W1750894760_1	25/06/2013	22:43:45	CB2	37.7	19	59	66
2083	W1750902731_1	27/06/2013	00:56:36	CB2	38.7	19	58	61
2084	W1753228269_1	22/07/2013	22:55:19	CB2	52.2	19	50	90
2084	W1753232512_1	23/07/2013	00:06:00	CB2	52.1	19	51	88
2084	W1753314559_1	23/07/2013	22:53:28	CB3	212.9	19	54	53
2084	W1753314670_1	23/07/2013	22:55:20	CB2	53.2	19	54	53
2084	W1753316386_1	23/07/2013	23:23:56	CB2	53.3	19	53	52
2084	W1753319710_1	24/07/2013	00:19:20	CB2	53.4	19	53	51
2084	W1753320748_1	24/07/2013	00:36:37	CB3	213.9	19	53	50
2084	W1753323916_1	24/07/2013	01:29:25	CB2	53.6	19	52	49
2084	W1753314577_1	24/07/2013	22:53:46	VIO	212.9	19	54	53
2084	W1753314629_1	24/07/2013	22:54:38	MT2	106.5	19	54	53
2086	W1764228800_1	27/11/2013	06:36:20	CB2	101.2	20	49	60
2086	W1764233960_1	27/11/2013	08:02:20	CB2	100.5	20	48	60

2086	W1764259760_1	27/11/2013	15:12:20	CB2	96.9	20	47	56
2086	W1764264921_1	27/11/2013	16:38:21	CB2	96.1	20	47	55
2088	W1769042808_1	21/01/2014	23:49:18	CB2	159.7	21	41	101
2088	W1769288270_1	24/01/2014	20:00:18	CB2	173.0	21	40	64
2088	W1769331470_1	25/01/2014	08:00:18	CB2	146.1	21	48	83
2088	W1769461071_1	26/01/2014	20:00:18	CB2	142.8	21	49	44
2090	N1775154439_1	02/04/2014	17:29:10	RED	13.4	22	38	44
2090	N1775154495_1	02/04/2014	17:30:06	BL2	13.4	22	38	44
2090	N1775154567_1	02/04/2014	17:31:18	UV3	13.4	22	38	44
2090	N1775154914_1	02/04/2014	17:37:05	GRN	13.4	22	38	44
2090	N1775155019_1	02/04/2014	17:38:50	MT2	13.4	22	38	44
2090	N1775155245_1	02/04/2014	17:42:36	CB2	13.4	22	38	44
2090	N1775157571_1	02/04/2014	18:21:29	CB2	13.3	21	37	44
2091	N1789048655_1	10/09/2014	12:56:57	UV2	15.7	23	37	49
2091	N1789049736_1	10/09/2014	13:15:58	RED	15.7	23	37	49
2091	N1789049792_1	10/09/2014	13:16:47	BL2	15.7	23	37	49
2091	N1789050291_1	10/09/2014	13:25:13	GRN	15.7	23	37	49
2091	N1798050396_1	10/09/2014	13:26:58	MT2	15.7	23	37	49
2091	N1789050622_1	10/09/2014	13:30:44	CB2	15.7	23	37	49
2091	N1789053342_1	10/09/2014	14:16:01	CB2	15.7	23	37	48